iScience

CellPress
OPEN ACCESS

Article

Targeting androgen regulation of TMPRSS2 and ACE2 as a therapeutic strategy to combat COVID-19

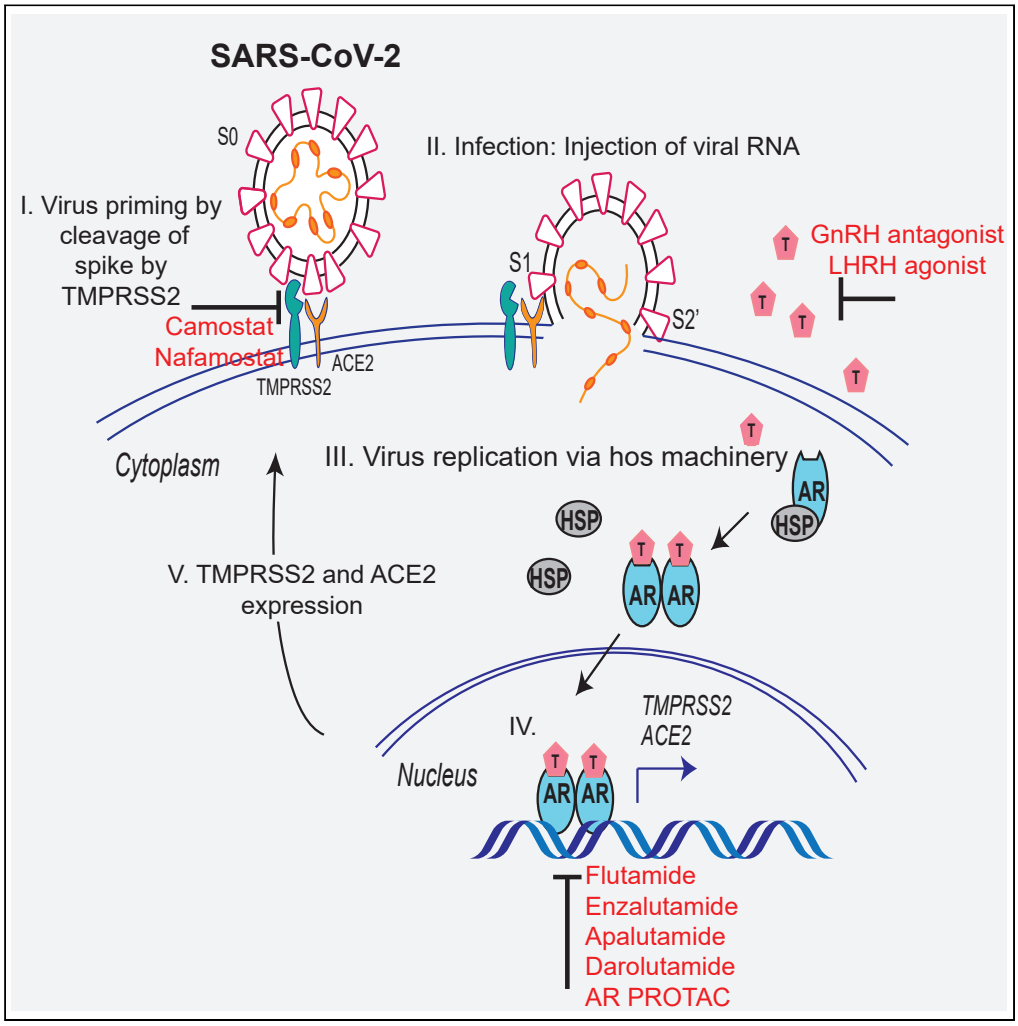

Qu Deng, Reyaz ur Rasool, Ronnie M. Russell, Ramakrishnan Natesan, Irfan A. Asangani

asangani@upenn.edu

HIGHLIGHTS

Androgen regulates the expression of SARS-Cov-2 receptor ACE2 and TMPRSS2

TMPRSS2 interacts with ACE2 in prostate and lung cells

Camostat blocks TMPRSS2-mediated cleavage of SARS-Cov-2 Spike

Androgen deprivation or AR antagonists attenuate SARS-CoV-2 Spike-mediated cell entry

Deng et al., iScience 24, 102254
March 19, 2021
https://doi.org/10.1016/j.isci.2021.102254

iScience

CellPress
OPEN ACCESS

Article

Targeting androgen regulation of TMPRSS2 and ACE2 as a therapeutic strategy to combat COVID-19

Qu Deng,[1,4] Reyaz ur Rasool,[1,4] Ronnie M. Russell,[2] Ramakrishnan Natesan,[1] and Irfan A. Asangani[1,3,5,*]

SUMMARY

Epidemiological data showing increased severity and mortality of COVID-19 in men suggests a potential role for androgen in SARS-CoV-2 infection. Here, we present evidence for the transcriptional regulation of SARS-CoV-2 host cell receptor ACE2 and TMPRSS2 by androgen in mouse and human cells. Additionally, we demonstrate the endogenous interaction between TMPRSS2 and ACE2 in human cells and validate ACE2 as a TMPRSS2 substrate. Furthermore, camostat—a TMPRSS2 inhibitor—blocked the cleavage of pseudotype SARS-CoV-2 surface Spike without disrupting TMPRSS2-ACE2 interaction, thus providing evidence for the first time of a direct role of TMPRSS2 in priming the SARS-CoV-2 Spike, required for viral fusion to the host cell. Importantly, androgen-deprivation, anti-androgens, or camostat attenuated the SARS-CoV-2 S-mediated cellular entry. Together, our data provide a strong rationale for clinical evaluations of TMPRSS2 inhibitors and androgen-deprivation therapy/androgen receptor antagonists alone or in combination with antiviral drugs as early as clinically possible to prevent COVID-19 progression.

INTRODUCTION

The ongoing COVID-19 (coronavirus disease 2019) pandemic caused by severe acute respiratory syndrome coronavirus 2 (SARS-CoV-2) infection is a global health crisis (Morens and Fauci, 2020; Wang et al., 2020). As of January 2021, over 100 million cases of COVID-19 and more than 2 million deaths have been recorded (https://coronavirus.jhu.edu). Epidemiological data have shown that males are disproportionally affected, being slightly more likely to be infected than females and accounting for most severely ill cases and higher fatality (https://globalhealth5050.org). This is compounded by older age and comorbidities such as diabetes, cardiovascular diseases, obesity, hypertension, and cancer (Williamson et al., 2020). This sex disparity with respect to increased morbidity and mortality in men suggests a potential role for the male hormone androgen in SARS-CoV-2 infection and host response (Stopsack et al., 2020; Wadman, 2020). The host immune response to SARS-CoV-2 potentiates a hyper-inflammatory cytokine storm involving the upregulation of tumor necrosis factor-α (TNF- α), interleukin 1β (IL-1 β), interleukin-6 (IL-6), monocyte chemoattractant protein-1 (MCP-1), and macrophage inflammatory protein 1-α (MIP1α), which is associated with COVID-19 severity and mortality (Mehta et al., 2020; Moore and June, 2020; Vabret et al., 2020; Zhang et al., 2020). Tumor cell-intrinsic and microenvironment-associated immune cell response to inflammation promotes the development and progression of several types of solid cancer, including prostate cancer (de Bono et al., 2020). Therefore, it is reasonable to hypothesize that the inflammatory signaling accompanying severe COVID-19 disease could cause cancer progression. Therefore, early intervention of COVID-19 management should be considered in patients with cancer who are more susceptible to SARS-CoV-2 infection due to their immunosuppressive state.

SARS-CoV-2 entry into the host cell is mediated by trimers of the transmembrane spike (S) glycoprotein. The S trimer binds to the cellular receptor angiotensin-converting enzyme 2 (ACE2) on the surface of target cells and mediates subsequent viral uptake and fusion dependent on processing by host proteases (Hoffmann et al., 2020c). Several host proteases, including TMPRSS2, cathepsin B and L, and furin have been suggested to promote the entry of SARS-CoV-2; how they process the Spike protein remains to be determined (Coutard et al., 2020; Shang et al., 2020; Walls et al., 2020). In relevant target cells, the cleavage of S by TMPRSS2 activates the protein for membrane fusion via extensive, irreversible conformational changes

[1]Department of Cancer Biology, Perelman School of Medicine, University of Pennsylvania, 421 Curie Boulevard, BRBII/III, Philadelphia, PA 19104, USA

[2]Department of Microbiology, University of Pennsylvania, 421 Curie Boulevard, BRBII/III, Philadelphia, PA 19104, USA

[3]Department of Cancer Biology, Abramson Family Cancer Research Institute, Epigenetics Institute, Perelman School of Medicine, University of Pennsylvania, 421 Curie Boulevard, BRBII/III, Philadelphia, PA 19104, USA

[4]These authors contributed equally

[5]Lead contact

*Correspondence: asangani@upenn.edu

https://doi.org/10.1016/j.isci.2021.102254

(Millet and Whittaker, 2015; Walls et al., 2017, 2020). As a result, SARS-CoV-2 entry into susceptible cells is a complex process that requires the concerted action of ACE2 receptor binding and TMPRSS2 proteolytic processing of the S protein to promote virus-cell fusion. Despite their well-documented role in SARS-CoV-2 entry, the nature of endogenous ACE2 and TMPRSS2 interactions in host cells is lacking.

TMPRSS2 is a widely studied androgen-regulated gene associated with prostate cancer (Afar et al., 2001). It contributes to prostate cancer pathogenesis by aberrantly driving oncogenic transcription. More than half of all prostate cancers in men of European ancestry harbor a gene fusion that juxtaposes the androgen receptor (AR) regulatory promoter/enhancer elements of *Tmprss2* in front of the ETS family transcription factors, most commonly *Erg* (Tomlins et al., 2005). Although ERG is not normally regulated by androgen, this somatic gene rearrangement results in oncogenic ERG expression under androgen receptor signaling. Furthermore, TMPRSS2 is known to promote metastatic spread of prostate cancer through HGF activation (Lucas et al., 2014). ACE2 is a zinc-dependent metalloprotease and is expressed at high levels in the heart, testis, and kidney and at lower levels in various tissues (Gheblawi et al., 2020). Therefore, identifying the molecular mechanisms governing the expression of TMPRSS2 and ACE2 could potentially explain the observed disparity in SARS-CoV-2 infection-associated morbidity and mortality in men.

In this study, we provide evidence for the AR-mediated transcriptional regulation of TMPRSS2 and ACE2 in mice and human prostate and lung cells. Specifically, androgen deprivation in mice by castration, or anti-androgen treatment *in vitro*, led to a reduction in TMPRSS2 and ACE2 transcript and protein levels. Furthermore, TMPRSS2 and ACE2 were found to interact in *cis* in prostate and lung cells, and the inhibition of TMPRSS2 protease activity by camostat blocked Spike priming. Finally, androgen deprivation, anti-androgens, or camostat treatment attenuated the SARS-CoV-2 pseudotype entry in lung and prostate cells, suggesting that these drug combinations could be effective in attenuating COVID-19 disease progression in men with or without prostate cancer.

RESULTS

Systemic androgen deprivation affects TMPRSS2 and ACE2 expression in mice

The poor clinical outcome of COVID-19 in men suggests a potential underlying androgen-related cause. The role of male sex hormone androgen in regulating the SARS-CoV-2 host cell receptor ACE2 and co-receptor TMPRSS2 has been speculated (La Vignera et al., 2020; Stopsack et al., 2020; Wadman, 2020). To evaluate the effect of androgen deprivation on TMPRSS2 and ACE2 expression in major tissues that are the primary sites for SARS-CoV-2 infection (Ziegler et al., 2020), we performed surgical castration in adult male mice (n = 3). One week post-castration, we harvested the lung, small intestine, heart, and kidney for qRT-PCR, immunoblotting, and immunohistochemistry analysis. Seminal vesicles and prostate were used as positive controls for systemic androgen deprivation. Tissues from the corresponding mock castrated males (n = 3) and females (n = 3) served as controls (Figure 1A). First, we determined the expression of *Tmprss2, Ace2,* and *Ar* in the control tissues. Each was expressed at varying degrees, with *Ar* and *Tmprss2* being the highest in seminal vesicles and *ACE2* in the small intestine (Figure S1A). Interestingly, a survey of adult human male tissue mRNA expression via bulk RNA-seq from the GTEx consortium (GTEx Consortium et al., 2017) demonstrated a similar expression pattern in prostate and small intestine for *AR*, *TMPRSS2*, and *ACE2* (Figure S1B), suggesting a potentially identical mechanism of regulation in man and mice. Next, as expected, the *Tmprss2* expression was highly androgen responsive in the seminal vesicles of the castrated males compared with the control males (Figure 1B). Except for the small intestine and the lung that showed a slight downward trend, levels of *Tmprss2* in the heart (with very low basal expression) and the kidney did not display any change upon castration. However, *Ace2* expression displayed a significant downregulation in the lung and the small intestine, which was similar to the levels found in female mice, and upregulation in the kidney tissues in the castrated male compared with controls. Remarkably, *Ace2* expression was also reduced in the hormone-sensitive seminal vesicles upon castration (Figure 1B), suggesting a potential role for androgen in regulating *Ace2* expression in these tissues. In concordance with the transcripts, the immunoblot analysis using total protein extracts from tissues demonstrated a reduced TMPRSS2 and ACE2 protein levels in the lung and the small intestine. The reduction in protein levels was much more dramatic than the transcript levels. In contrast, the kidney tissue displayed an increase in the ACE2 protein, but not TMPRSS2, corroborating the transcript data (Figure 1C). Next, we performed immunohistochemistry to identify the specific cell types in these tissues that display altered expression for TMPRSS2 and ACE2 proteins upon androgen deprivation. In these experiments, DU145 and VCaP prostate cancer xenograft tissues served as a negative control for AR, TMPRSS2, and ACE2, respectively, which showed

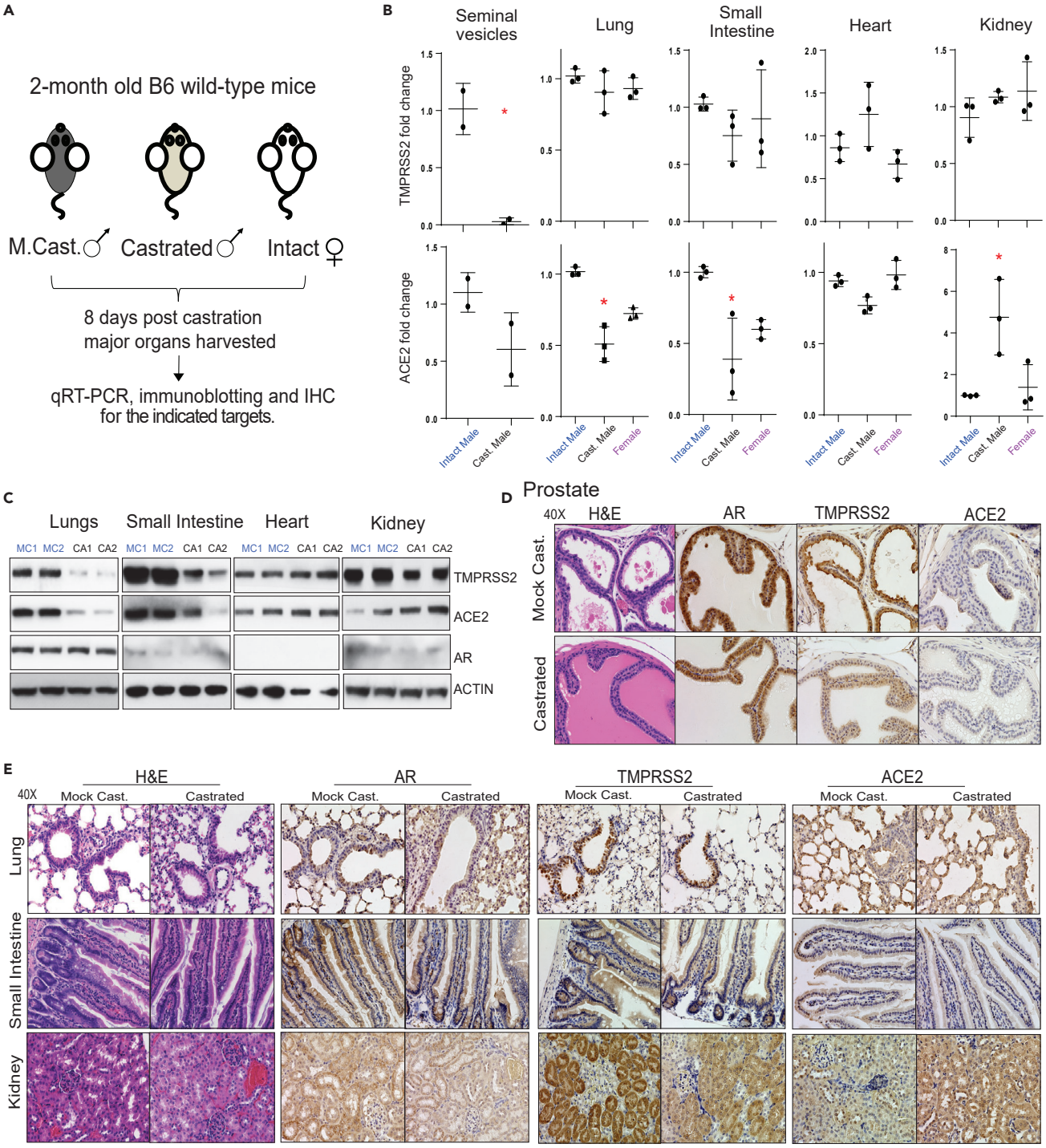

Figure 1. Effect of androgen deprivation by castration on the expression of TMPRSS2 and ACE2 in adult male mice

(A) Schematic depicting the castration experiment in 8- to 9-week-old wild-type C57BL/6J mice.

(B) Varying effect of systemic androgen deprivation on the transcription of TMPRSS2 and ACE2 in major organs. qRT-PCR analysis for TMPRSS2 and ACE2 transcripts in the indicated organs from mock, castrated male and normal females. Highly hormone-responsive seminal vesicles from the male mice served as a positive control for the effect of androgen deprivation on the target genes.

(C) Immunoblot analysis showing the levels of TMPRSS2, ACE2, and AR proteins in the indicated organs from two separate mock versus castrated males. β-Actin served as a loading control.

Figure 1. *Continued*

(D) Immunohistochemistry analysis of the indicated target protein in the prostate from mock and castrated males. Note the reduced TMPRSS2 staining in the castrated group and lack of/sparse ACE2 staining in both groups.

(E) As in (D) for the indicated organs. Staining for AR was observed in all the tested organs. Note the reduced TMPRSS2 staining in the bronchial epithelium of lung, columnar epithelium of small intestine, and proximal convoluted tubules in the kidney, in the castrated group. Also, note the reduced ACE2 staining in alveolar epithelium of the lungs and columnar epithelium of small intestine and increased staining in the kidney from the castrated group. Also, see Figures S1 and S2. *$p < 0.05$ (Student's t test).

a clear lack of staining (Figure S2A). As expected, based on the transcript data, reduced staining for TMPRSS2, ACE2, and AR protein in hormone-sensitive seminal vesicles was observed in the castrated group (Figure S2B). Furthermore, the hormone-responsive prostate luminal epithelial cells showed reduced staining for AR and TMPRSS2 in response to castration (Figure 1D). We also observed a small minority population of epithelial cells with <5% staining for ACE2 on the apical surface of the prostate epithelium, which was absent in the castrated group. The identical minimal co-expression pattern of ACE2 and TMPRSS2 was also identified in human prostate tissues, where club cells that constitute a mere 0.07% of total prostate epithelial cells and resemble club cells in the lung were double-positive (Henry et al., 2018; Montoro et al., 2018; Song et al., 2020). We observed no morphological changes in response to castration in lung, small intestine, and kidney tissue through H&E staining. Similar to transcripts, the AR, ACE2, and TMPRSS2 proteins were detected in all the tested tissue types at varying degrees (Figure 1E). A strong staining for TMPRSS2 was detected exclusively in the lung respiratory bronchiole epithelium, with minimal staining of type II alveolar cells, which is consistent with the expression pattern observed in human tissue (Stopsack et al., 2020). The staining intensity, especially in type II alveolar cells, was reduced in the castrated group. The ACE2 staining could be observed in the lung parenchyma; both type I and type II alveolar cells and the bronchiole epithelium apical surface of the castrated males showed relatively lower expression (Figures 1E and S2C). Next, the small intestine mucosa from the control group showed positive cytoplasmic and nuclear AR staining, which was reduced in the castrated group. TMPRSS2 displayed high staining in the crypt and lower portion of the villi with the exception of the goblet cells, and the staining gradually diminished on top of the villi. ACE2 was mainly present on the apical surface of the enterocytes on the top part of the villi. These expression patterns mirror data from human small intestinal tissue, especially ileum and jejunum (Hamming et al., 2004; Ziegler et al., 2020). The abundance of double-positive cells was largely reduced in the castrated male tissue due to the reduction in both ACE2 and TMPRSS2 levels. Concerning the kidney, the AR staining was detected in the tubular cells, which was reduced upon castration. TMPRSS2 showed positivity mainly in the proximal tubules compared with other cells, which was reduced in the castrated group (Muus et al., 2020). Finally, a homogeneous ACE2 expression was detected across kidney tissue on the apical surface of the tubular cells. In line with the kidney's role in the renin-angiotensin-aldosterone system, the ACE2 intensity was strongly elevated in the castrated males responding to reduced blood pressure brought out by androgen deprivation (Dubey et al., 2002). Together, these analyses clearly demonstrate that the androgen deprivation has an effect on the expression of TMPRSS2 and ACE2, particularly in the lung, small intestine, and kidney. Although there was a discrepancy concerning transcript and protein levels of TMPRSS2 in the tested tissues—particularly in the kidney—post-transcriptional regulation of TMPRSS2 by androgen-regulated microRNA could not be ruled out (Nersisyan et al., 2020).

AR regulates TMPRSS2 and ACE2 expression in human prostate and lung cells

The observation that systemic androgen deprivation affects the expression of TMPRSS2 and ACE2 in hormone-sensitive tissues such as prostate and seminal vesicles, and also in major organs such as the lungs, small intestine, and kidney, led us to investigate the direct role of AR in the transcriptional regulation of these two critical genes beyond the prostate. Although the upstream enhancer of *Tmprss2* is a well-known target for AR (Asangani et al., 2014), we sought to identify whether regulatory elements of *Ace2* are also occupied by AR. We analyzed publicly available AR chromatin immunoprecipitation (ChIP)-seq data for AR-binding sites within 50 kb of the transcription start sites (TSSs) of the *Tmprss2* and *Ace2* genes in mouse prostate, comparing castration and castration followed by testosterone injection for 3 days (Pihlajamaa et al., 2014). As expected, multiple AR peaks were observed in the upstream of the *Tmprss22* TSS in the testosterone-treated prostate, which was also present in DHT (dihydrotestosterone)-treated VCaP and LNCaP human prostate cell lines (Figure 2A). Interestingly, the upstream region of *ACE2* also showed AR binding in mouse as well as in human prostate cells (Figures 2A and S3A). Motif analysis of the AR-occupied regions revealed the presence of androgen response elements (AREs), as well as binding sites for other steroid receptors such as GR (glucocorticoid receptor) and PR (progesterone receptor), and

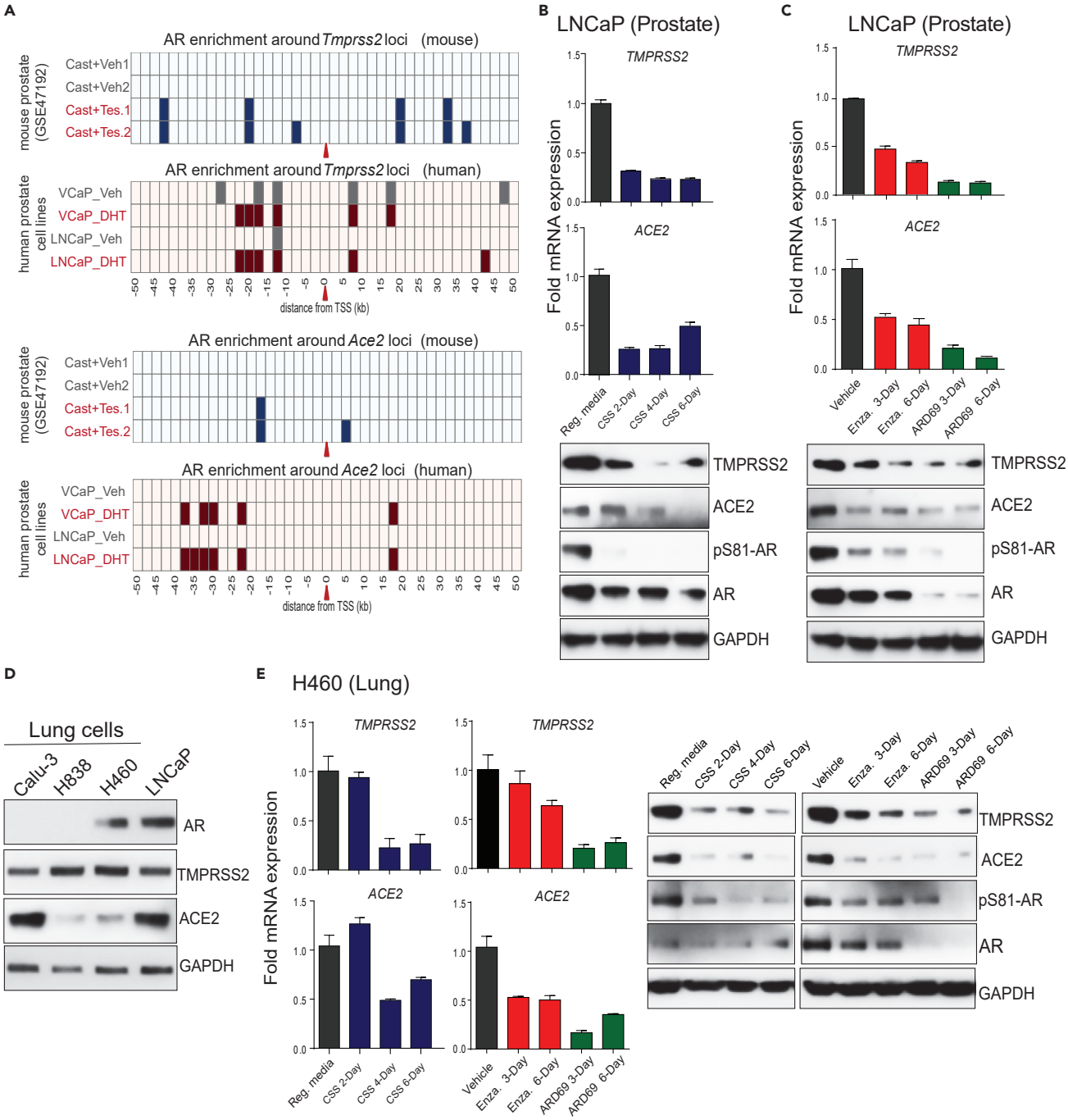

Figure 2. AR-mediated transcriptional regulation of TMPRSS2 and ACE2 in human prostate and lung cells

(A) TMPRSS2 and ACE2 loci display enhanced AR binding upon testosterone stimulation. Shown are AR ChIP-seq peaks around TMPRSS2 and ACE2 loci (the red arrow indicates the TSS) in the vehicle and testosterone-treated conditions in mouse prostate tissue (GSE47192) and human prostate cell lines.

(B-C) Androgen deprivation, anti-androgen, or AR degradation results in the loss of TMPRSS2 and ACE2 expression. Top, qRT-PCR analysis for TMPRSS2 and ACE2 transcripts in human prostate cells, LNCaP, grown in the indicated conditions; Reg. media: regular media with 10% serum, CSS: charcoal striped serum, Enza: Enzalutamide at 25 μM, ARD69: AR degrader at 250nM. Bottom, immunoblot analysis for the indicated protein. GAPDH was used the loading control.

(D) Immunoblot showing the expression of AR, TMPRSS2, ACE2, and GAPDH proteins in a panel of human lung cell lines; LNCaP was used as the positive control.

(E) qRT-PCR and immunoblot analysis as in (B and C) for human lung cell line H460. Also see Figure S3.

pioneering factor such as FOXA1 (Figure S3A), suggesting potential regulation of ACE2 by other steroid hormones. Next, we wanted to investigate whether TMPRSS2 and ACE2 expression in human cells responds to androgen deprivation or anti-androgen treatment. We cultured LNCaP cells in steroid-deprived conditions for 2, 4, and 6 days and assessed the expression of TMPRSS2 and ACE2 compared with cells grown in steroid-proficient condition. As one of the most androgen-responsive gene, TMPRSS2 transcript and protein levels showed downregulation in the steroid-deprived cells compared with their steroid-proficient controls (Figure 2B). This was accompanied by a concomitant decrease in the levels of phosphoSer81-AR (pAR), an active chromatin-bound form of AR (Rasool et al., 2019). More importantly, the ACE2 transcript and the protein levels were also downregulated in the steroid-deprived cells. Treatment with the second-generation anti-androgen enzalutamide or AR degrader ARD-69 (Han et al., 2019) led to a time-dependent reduction in the TMPRSS2 and ACE2 expression that was accompanied by reduced pAR levels in LNCaP cells (Figure 2C). As lung is one of the primary site of SARS-CoV-2 infection causing severe disease, we tested whether lung cells respond to androgen deprivation and anti-androgen treatment with respect to the expression of TMPRSS2 and ACE2. First, we screened a panel of lung cancer cell lines and found H460 cells positive for AR, TMPRSS2, and ACE2 (Figure 2D). Similar to that observed in LNCaP cells, H460 displayed a marked downregulation of TMPRSS2 and ACE2 accompanied by reduced pAR levels upon androgen deprivation, or AR-targeted therapy (Figure 2E). In a complementary experiment, stimulation with DHT in LNCaP and H460 cells led to increased pAR and concomitant increase in TMPRSS2 and ACE2 protein levels (Figure S3B). Interestingly, androgen-induced AR-dependent upregulation of TMPRSS2 has been demonstrated in other lung cancer cell lines (Mikkonen et al., 2010). These data clearly demonstrate a potential role of AR in regulating SARS-CoV-2 receptor and co-receptor in prostate and lung cells.

TMPRSS2 interacts with ACE2 in prostate and lung cells

Having identified the androgen dependency of TMPRSS2 and ACE2 expressions *in vivo* in mice and *in vitro* in human cell lines, we turned our attention to their function concerning SARS-CoV-2 Spike (SARS-2-S) priming. Although TMPRSS2 is implicated in priming of SARS-2-S protein (Hoffmann et al., 2020c), it is unclear whether this occurs in association with ACE2. Furthermore, TMPRSS2-mediated enhancement of SARS virus entry has been shown to accompany ACE2 cleavage (Shulla et al., 2011). Therefore, we studied whether TMPRSS2 and ACE2 physically associate in an endogenous setting and examined the effect of TMPRSS2 protease inhibition on their interaction and cleavage of ACE2. TMPRSS2 is composed of a cytoplasmic region (amino acid [aa] 1–84), a transmembrane region (aa 85–105), and an extracellular region (aa 106–492). The latter is composed of three domains: the LDLRA (LDL receptor class A) domain (residues 112–149), which forms a binding site for calcium; the SRCR (scavenger receptor cysteine-rich) domain (aa 149–242), involved in the binding to other cell surface or extracellular proteins; and the Peptidase S1 domain (aa 256–489), which contains the protease active site: residues H296, D345, and S441 (Figure 4A). An auto-cleavage site at aa 255–256 has been shown to allow shedding of the extracellular region of TMPRSS2 (Afar et al., 2001). The ACE2 protein is 805 aa long and is composed of a short cytoplasmic region, a transmembrane region, and an extracellular N-terminal region that contain zinc metallopeptidase domain (Figure 3A). TMPRSS2-mediated cleavage of ACE2 at its N terminus (residues 697 to 716) was shown to be required for ACE2 to interact with SARS-S protein in 293T overexpression system (Heurich et al., 2014; Shulla et al., 2011). Our experiments show that overexpression of TMPRSS2 in HEK293-T cells that stably express ACE2 led to ACE2 cleavage, resulting in reduced levels of the ~120-kDa full-length form and increased levels of a ~20-kDa C-terminal fragment (Figure 3B), as previously documented (Shulla et al., 2011). Importantly, the treatment of cells with camostat, a TMPRSS2 serine protease inhibitor (Kawase et al., 2012) (Figure 3C), entirely blocked ACE2 cleavage, suggesting ACE2 as a *bona fide* substrate of TMPRSS2 (Shulla et al., 2011). Intriguingly, camostat treatment did not result in any change in ACE2 full-length levels in LNCaP cells (Figure S4A). This observation led us to address the existence of TMPRSS2-ACE2 complex in the endogenous setting. Toward that, we determined the physical interaction between TMPRSS2 and ACE2 protein using N- and C-terminal-specific antibodies (Figure 3A). Reciprocal immunoprecipitation experiments showed an endogenous association between TMPRSS2 and ACE2 in LNCaP prostate cells (Figure 3D). Likewise, Calu-3 lung cells demonstrated a physical interaction between TMPRSS2 and ACE2 (Figure 3E). Along with the full-length 50-kDa TMPRSS2, a smaller approximately 38-kDa variant was found to interact with ACE2 prominently in both the cell lines. Notably, the treatment of cells with camostat did not reduce the amount of ACE2 being pulled down by TMPRSS2, and vice versa, suggesting the endogenous TMPRSS2-ACE2 complex to be stable and not dependent on proteolytic cleavage. A similar endogenous

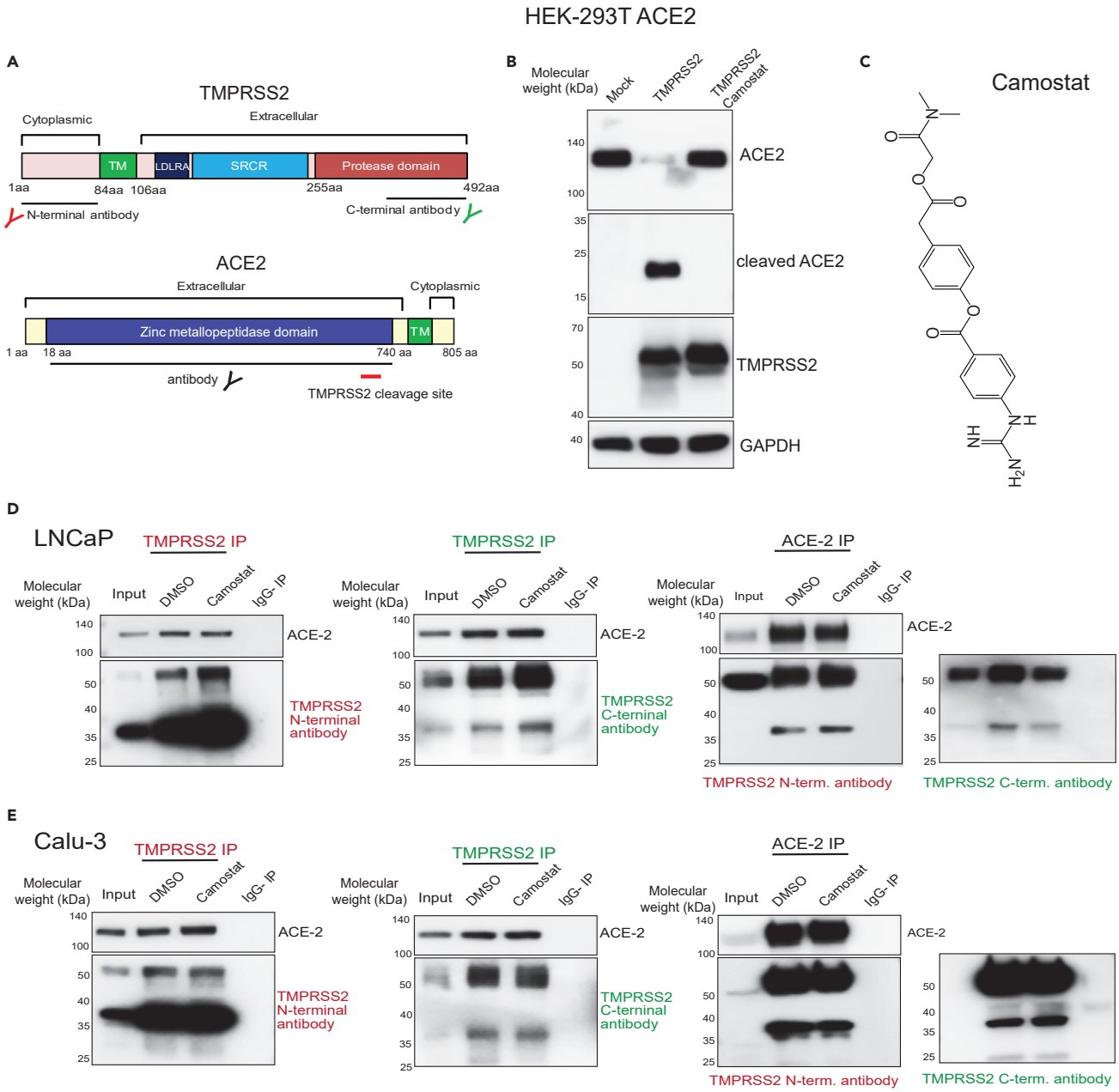

Figure 3. TMPRSS2 physically interacts with ACE2 in prostate and lung cells

(A) Schematic showing the domain structure of human TMPRSS2 and ACE2 protein. The TMPRSS2 cleavage site on ACE2 is shown with red bar. Epitopes recognized by the antibodies used in the immunoprecipitation are indicated.

(B) TMPRSS2 cleaves ACE2. HEK 293T ACE2 cells were transfected with TMPRSS2-encoding plasmid, and 6 h post transfection the cells were treated with DMSO or camostat (250 μM). 48h post-transfection, proteins were extracted and used for immunoblotting with anti-ACE2, anti-TMPRSS2, and anti-GAPDH antibody.

(C) Chemical structure of camostat.

(D) TMPRSS2 and ACE2 physically interact and are not disrupted by camostat, a TMPRSS2 inhibitor. Reciprocal immunoprecipitation using the indicated antibodies with LNCaP protein extracts. Cells were treated with DMSO or camostat (250 μM) for 24 h followed by protein extraction. Note, along with the full-length ~50-kDa TMPRSS2 protein, the presence of a novel approximately 38-kDa cleaved form detected in both N- and C-terminal TMPRSS2 antibody pull down and ACE2 pull down. IgG pull down served as a negative control; inputs were 5%–10%.

(E) As in (D) with Calu-3 protein extracts. Also see Figure S4.

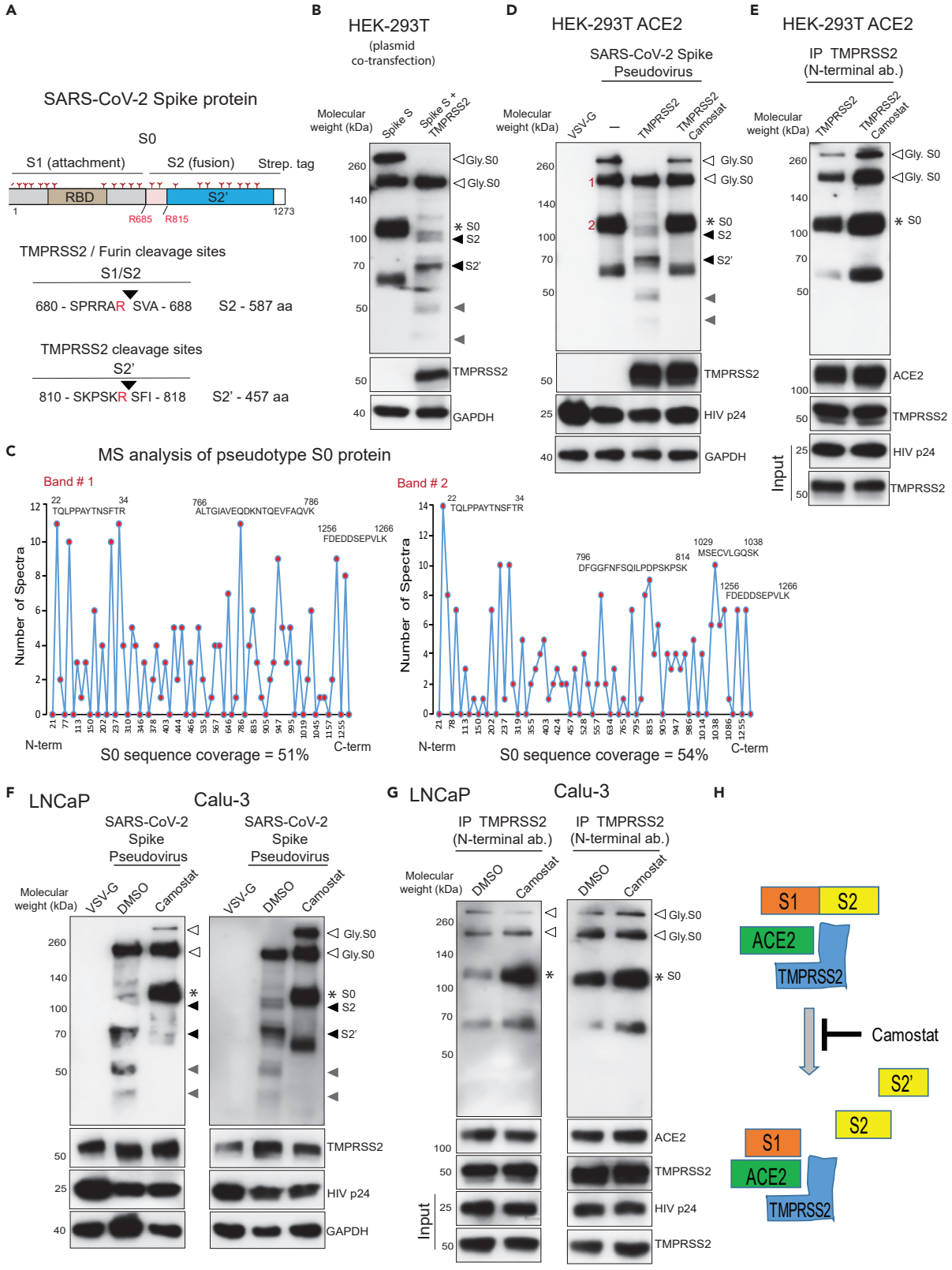
A
SARS-CoV-2 Spike protein
S0
S1 (attachment)
S2 (fusion)
Strep. tag
RBD
S2'
1
R685
R815
1273
TMPRSS2 / Furin cleavage sites
S1/S2
680 - SPRRAR SVA - 688
S2 - 587 aa
TMPRSS2 cleavage sites
S2'
810 - SKPSKR SFI - 818
S2' - 457 aa
B
HEK-293T
(plasmid
co-transfection)
Molecular weight (kDa)
Spike S
Spike S + TMPRSS2
Gly.S0
S0
S2
S2'
TMPRSS2
GAPDH
D
HEK-293T ACE2
SARS-CoV-2 Spike
Pseudovirus
Molecular weight (kDa)
VSV-G
TMPRSS2
TMPRSS2 Camostat
Gly.S0
S0
S2
S2'
TMPRSS2
HIV p24
GAPDH
E
HEK-293T ACE2
IP TMPRSS2
(N-terminal ab.)
Molecular weight (kDa)
TMPRSS2
TMPRSS2 Camostat
Gly. S0
S0
ACE2
TMPRSS2
HIV p24
TMPRSS2
Input
C
MS analysis of pseudotype S0 protein
Band # 1
TQLPPAYTNSFTR
ALTGIAVEQDKNTQEVFAQVK
FDEDDSEPVLK
Number of Spectra
N-term
C-term
S0 sequence coverage = 51%
Band # 2
TQLPPAYTNSFTR
DFGGFNFSQILPDPSKPSK
MSECVLGQSK
FDEDDSEPVLK
Number of Spectra
N-term
C-term
S0 sequence coverage = 54%
F
LNCaP
Calu-3
SARS-CoV-2 Spike Pseudovirus
Molecular weight (kDa)
VSV-G
DMSO
Camostat
Gly.S0
S0
S2
S2'
TMPRSS2
HIV p24
GAPDH
G
LNCaP
Calu-3
IP TMPRSS2 (N-terminal ab.)
Molecular weight (kDa)
DMSO
Camostat
Gly.S0
S0
ACE2
TMPRSS2
HIV p24
TMPRSS2
Input
H
S1
S2
ACE2
TMPRSS2
Camostat
S2'
S2
S1
ACE2
TMPRSS2

Figure 4. TMPRSS2 in complex with ACE2 cleaves SARS-CoV-2 Spike protein

(A) Schematic representation of the expression construct of full-length SARS-CoV-2 spike (S0) protein that has S1 and S2 segments involved in virus attachment and fusion, respectively. Segments of S1 include RBD - receptor-binding domain, and S1/S2 cleavage site; S2 has an S2′ cleavage site. Tree-like symbol denotes glycans, and the C terminus contains 2x Strep-tag. The TMPRSS2 cleavage site on S1/S2 and S2′ site is indicated with the resulting length of the S2 and S2′ protein. Cleaved S2 and S2′ fragment lengths are shown.

(B) TMPRSS2 cleaves glycosylated SARS-2-S protein. HEK293T cells were transfected with SARS-2-S plasmid with or without TMPRSS2-encoding plasmid. 48 h post-transfection, proteins were extracted and used for immunoblotting with anti-streptavidin, anti-TMPRSS2, and anti-GAPDH antibody. The open arrow and * indicate the glycosylated and non-glycosylated uncleaved S0 protein, respectively. The filled black arrow indicates TMPRS2-cleaved S2 and S2′. The filled gray arrow indicates TMPRSS2-cleaved potential S2 and S2′ fragments arising from non-glycosylated S0.

(C) Mass spectrometric (MS) analysis of pseudotype-incorporated S0 protein. SARS-2-S pseudovirus was directly subjected to streptavidin immunoprecipitation (IP), followed by MS analysis for sequencing. Histograms show peptide coverage for the two prominent bands detected with in IP-western (See Figure S4).

(D) Pseudotype SARS-CoV-2 Spike is cleaved by TMPRSS2, which is blocked by camostat. HEK293T ACE2-overexpressing cells were transfected with TMPRSS2 plasmid; 48 h later cells were pretreated with 500 μM camostat for 4 h followed by pseudovirus inoculation by spinoculation for 1 h. Next, 4 h post-spinoculation recovery total lysates were prepared and used for immunoblotting with the indicated antibody. VSV-G-containing pseudotype virus served as a negative control, and HIVp24 served as a positive control for viral inoculation.

(E) Camostat blocks TMPRSS2-mediated cleavage of S0 without disrupting the interaction between TMPRSS2-ACE2-Spike S complex. Lysate from (C) was used to immunoprecipitate TMPRSS2 using N-terminal antibody followed by immunoblotting for the indicated target. Note the increased pull-down of uncleaved Spike S0 by the TMPRSS2 and the complete absence of S2, S2′, and other cleaved fragments in both DMSO and camostat lane.

(F) Camostat reverses the endogenous TMPRSS2-mediated Spike cleavage in human prostate and lung cells. The LNCaP and Calu-3 cells were pretreated with camostat (500 μM) for 4 h followed by pseudotype VSV-G or SARS-CoV-2 particle spinoculation for 1 h and processed as in (D).

(G) Camostat blocks TMPRSS2-mediated cleavage of S0 and S2 without disrupting the interaction between TMPRSS2-ACE2-Spike S complex in LNCaP and Calu-3 cells. Lysate from (C) was used to immunoprecipitate TMPRSS2 using N-terminal antibody followed by immunoblotting for the indicated target. Note the increased pull-down of Spike S0 by the TMPRSS2 and the lack of S2, S2′, and other fragments in the camostat lane.

(H) Schematic showing the interaction between Spike S, ACE2, and TMPRSS2 leading to cleavage of Spike S into S1, S2, and S2′ segments. S0/S1 continues to bind tightly through its RBD to ACE2, which is in complex with TMPRSS2, whereas upon cleavage the S2 and S2′ get dissociated from the TMPRSS2-ACE2 complex. Also see Figure S5.

ACE2-TMPRSS2 interaction was observed in AR-positive H460 lung cells (Figure S4B). These data demonstrate for the first time an endogenous association between TMPRSS2 and ACE2 in prostate and lung cells.

TMPRSS2 inhibition blocks S priming without affecting its interaction with ACE2

Next, we addressed the role of TMPRSS2 on priming of SARS-CoV-2 Spike (SARS-2-S), a heavily glycosylated transmembrane protein (Cai et al., 2020; Ke et al., 2020) (Figure 4A). The unprocessed Spike S0 protein encoded by the SARS-CoV-2 genome is 1,273 amino acids long. It is incorporated into the viral membrane and facilitates viral entry into target cells. Similar to SARS-CoV and MERS-CoV Spike proteins, SARS-CoV-2 Spike consists of a proprotein convertase motif at the S1/S2 boundary cleaved by furin protease and TMPRSS2 into two fragments, the receptor-binding fragment S1 and the membrane fusion fragment S2 (Hoffmann et al., 2020b, 2020c; Iwata-Yoshikawa et al., 2019; Shang et al., 2020; Shulla et al., 2011; Zhou et al., 2015). Although the role of TMPRSS2 in SARS-2-S priming has been suggested (Hoffmann et al., 2020c), direct evidence demonstrating the cleaving of SARS-2-S by endogenous TMPRSS2 is lacking. Therefore, we performed experiments to specifically address the role of ectopically expressed or endogenous TMPRSS2 in SARS-2-S activation. Transfection of codon-optimized plasmid encoding SARS-2-S protein and 2xStrep.tag (Gordon et al., 2020) in HEK293-T showed a distinct ~180-kDa and an ~280-kDa band, which is likely the differentially glycosylated S0 protein. The two other bands at ~120 kDa and at ~60 kDa could be the non-glycosylated fragments (Figure 4B). The S1 fragment could not be detected in the immunoblots as the streptavidin-tag is located at the C-terminal end of the constructs. The co-transfection with TMPRSS2 plasmid led to cleavage of S0 into distinct bands corresponding to S2 and S2′ (Figure 4B). Interestingly, the ~280-kDa and ~120-kDa bands were fully processed by TMPRSS2, suggesting that the S1/S2 site on glycosylated and non-glycosylated S0 protein could be equally targeted by TMPRSS2 for cleavage. The smaller fragments observed are most likely the TMPRSS2-cleaved S2 and S2′ from the non-glycosylated S0. To further demonstrate the action of TMPRSS2 on S activation, we performed spinoculation with pseudotype virus that contains replication-deficient human immunodeficiency virus (HIV) particles bearing SARS-2-S proteins in TMPRSS2-negative HEK293-T ACE2 cells. First, the mass spectrometry-based sequencing of pseudotype-incorporated SARS-2-S identified the prominent ~180-kDa and ~120-kDa fragments as full-length S0 proteins, suggesting the presence of uncleaved Spike on the pseudotype (Figures 4C, S5A, and S5B). Additionally, we tested and found that HEK293-T ACE2 cells have superior uptake of HIV pseudotype SARS-2-S compared with HEK293-T cells, confirming ACE2 as the major receptor SARS-CoV-2 (Figure S5C). In agreement with a recent study that demonstrated the existence of S mostly in the closed

uncleaved pre-fusion confirmation on the authentic SARS-CoV-2 (Turonova et al., 2020), the purified pseudotype SARS-2-S virus spinoculation followed by immunoblotting displayed both glycosylated ~180-kDa and non-glycosylated ~120-kDa full-length S0 protein (Figure 4D). Next, the cells transfected with TMPPSS2 plasmid showed clear processing of pseudotype full-length S0 into S2 and S2′. As expected, pretreatment with camostat prevented the TMPRSS2-mediated cleavage of pseudotype S0. As we had observed proteolytic cleavage of ACE2 by TMPRSS2 in the overexpression model (Figure 3B), we sought to observe whether the TMPRSS2-mediated cleavage of SARS-2-S is taking place in the presence of ACE2. Toward this, we performed immunoprecipitation of TMPRSS2 on pseudotype SARS-2-S spinoculation in the presence or absence of camostat. Increased pull-down of uncleaved full-length S0 was observed in the camostat-treated cells compared with control, due to the inhibition of TMPRSS2 protease activity and resulting lack of S priming (Figure 4E). Interestingly, the amount of ACE2 pulled down by TMPRSS2 was not affected by camostat, suggesting the SARS-2-S cleavage by TMPRSS2 is mediated in the presence of ACE2 in the complex. Noticeably, the cleaved S0 fragments were completely absent in the TMPRSS2 pull-down, suggesting that once processed, the S2 and S2′ fragments are released from the TMPRSS2-ACE2 complex. Similar observations of pseudotype SARS-2-S cleavage by endogenous TMPRSS2 in the presence of endogenous ACE2 were made with LNCaP and Calu-3 cells (Figures 4F and 4G). These data clearly demonstrate the crucial role played by TMPRSS2 in SARS-CoV-2 viral fusion to the host cell by Spike protein priming (Figure 4H).

Camostat alone or in combination with AR-directed therapies reduces SARS-2-S pseudovirus entry into prostate and lung cells

After identifying the role of androgen in regulating TMPRSS2 and ACE2 expression, and TMPRSS2-mediated SARS-2-S priming, we asked whether therapeutic intervention targeting AR and TMPRSS2 protease function could affect SARS-CoV-2 infection in prostate and lung cells. Replication-defective virus particles bearing SARS-2-S proteins faithfully reflect critical aspects of SARS-CoV-2 host cell entry (Hoffmann et al., 2020c). Therefore, we employed HIV pseudotypes bearing SARS-2-S and nano-luciferase reporter to test the efficacy of Camostat and AR-directed therapies in blocking cell entry (Figure 5A). We first asked whether androgen deprivation could affect pseudotype virus entry by reducing TMPRSS2 and ACE2 (Figure 2). LNCaP cells grown in the androgen-proficient condition were readily susceptible to the entry driven by SARS-2-S (Figure 5B). However, cells grown under steroid-deprived condition (CSS [charcoal stripped serum]) demonstrated a significant reduction in the entry of pseudotype virus. Interestingly, camostat treatment efficiently blocked the SARS-2-S-mediated entry only in the androgen-proficient condition, suggesting the presence of TMPRSS2 as a requirement for its potency. Next, we treated LNCaP cells grown in normal growth condition with anti-androgen enzalutamide, AR degrader ARD-69, or camostat and observed a significant reduction in SARS-2-S-driven entry compared with the DMSO control. Notably, the combination of camostat with enzalutamide or ARD-69 was more efficacious in blocking the entry than the single drug (Figure 5C). Since lungs are the primary target of SARS-CoV-2, we tested whether androgen deprivation, enzalutamide, ARD-69, and camostat could block SARS-2-S-mediated entry in AR-positive H460 cells. Similar to LNCaP cells, pseudovirus entry was significantly reduced in the H460 cells grown in the steroid-deprived condition, enzalutamide, and ARD-69 alone or in combination with camostat compared with the control (Figures 5D and 5E). As expected, compared with camostat, the enzalutamide or AR degrader treatment in AR-negative Calu-3 cells did not block the SARS-2-S-mediated entry (Figure 5F). Importantly, unlike SARS-2-S, HIV pseudotypes bearing VSV-G did not display any significant difference in cell entry under these conditions in all three tested cell lines (Figure S6). These results indicate that the treatment of AR-positive prostate and lung cells with AR-directed therapies in combination with TMPRSS2 inhibitor efficiently blocks SARS-2-S-mediated viral entry.

DISCUSSION

Early intervention of SARS-CoV-2 infection could prevent cytokine storm-mediated progression to severe pneumonia and multi-organ failure in patients with COVID-19 (Mehta et al., 2020). Although the source of the cytokine storm that causes multi-organ dysfunction is not yet clear, uncontrolled viral replication may contribute to COVID-19 severity and death. The present study provides evidence that the expression of SARS-CoV-2 host cell receptor ACE2 and co-receptor TMPRSS2 is regulated in part by the male sex hormone androgen. Furthermore, our data provide evidence that the cell entry of SARS-CoV-2 Spike pseudovirus can be blocked by androgen deprivation, anti-androgens, or clinically proven inhibitors of TMPRSS2. Although other studies have demonstrated the role of TMPRSS2 in SARS-CoV-2 Spike priming (Hoffmann et al., 2020c), we provide the first direct evidence for the endogenous interaction between

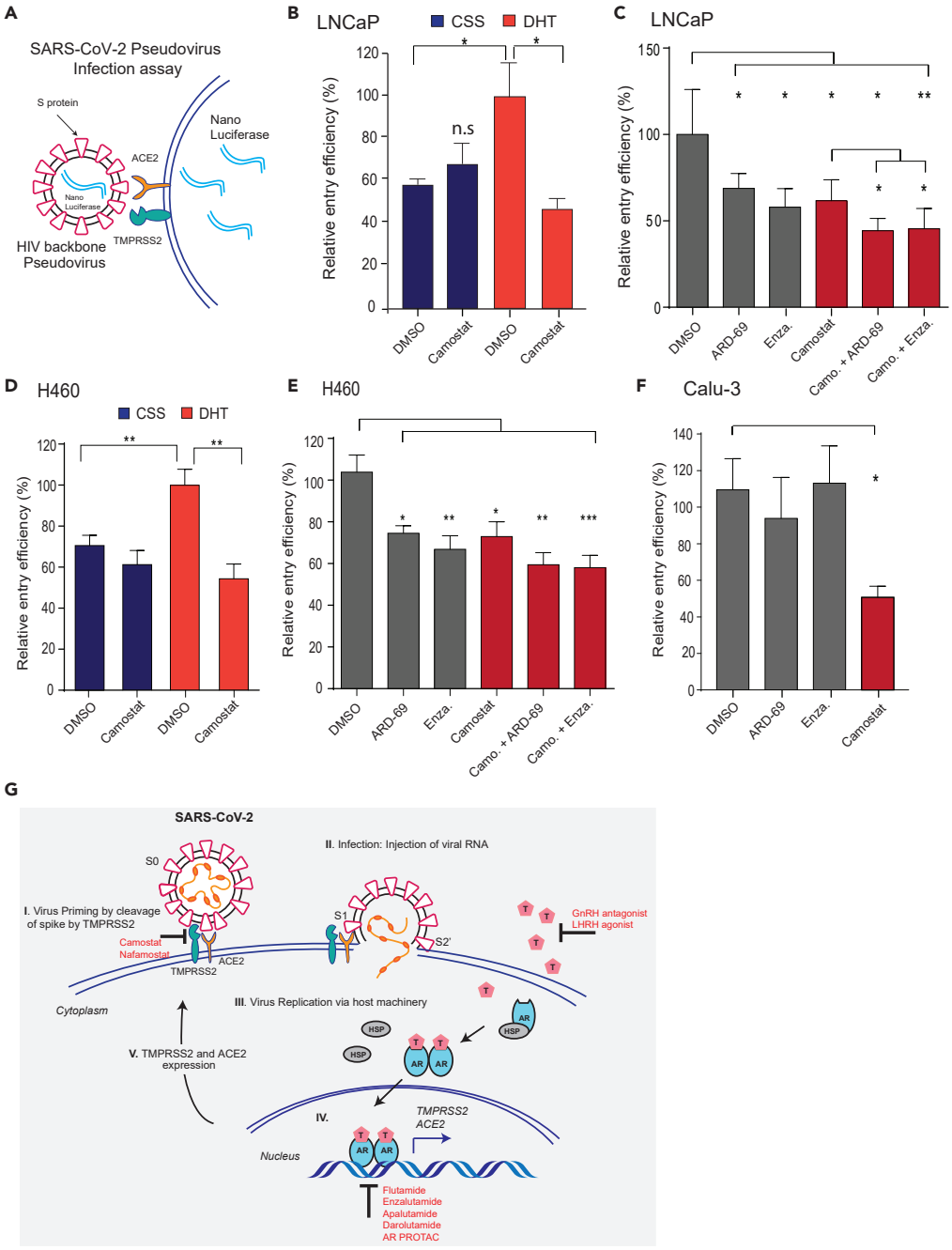

Figure 5. AR-targeted therapies in combination with camostat attenuates the entry of pseudotype SARS-CoV-2 into the host cells

(A) Schematic depicting the SARS-CoV-2 Spike S pseudovirus entry assay. The pseudotype consists of Spike S and nano-luciferase reporter.

(B) Androgen deprivation attenuates pseudotype entry. LNCaP cells grown in androgen-deprived serum-containing media for 3 days were pretreated with DMSO, DHT (10 nM), or camostat (300 μM) for 1 h followed by inoculation with SARS-CoV-2 Spike S pseudovirus; 24 h post-inoculation, the pseudovirus entry efficiency was measured by means of nano-luciferase signal accompanying entry. The entry efficiency in the DHT-treated cells was taken as 100%. Error bar indicates SEM (n = 5).

(C) Anti-androgens or AR degraders with or without camostat attenuate pseudovirus entry. LNCaP cells grown in complete media were pretreated with enzalutamide (10 μM) or ARD-69 (500 nM) alone, or in combination with camostat (300 μM) for 1 h followed by inoculation with pseudovirus; 24 h post-inoculation reporter activity measured as in (D).

Figure 5. *Continued*

(D and E) As in (C and D) with AR-positive H460 lung cells.

(F) AR-negative Calu-3 cells do not respond to anti-androgens. Calu-3 cells are pretreated with enzalutamide, ARD-69, or camostat followed by pseudovirus inoculation; 24 h later reporter signal characterizes the pseudovirus entry efficiency. Error bar indicates SEM (n = 5). *p < 0.05, **p < 0.005, ***p < 0.0005 (Student's t test).

(G) Schematic depicting the role of TMPRSS2 in SARS-CoV-2 Spike cleavage, and androgen-mediated expression of ACE2 and TMPRSS2 that could potentially be targeted by AR-directed therapies. Also see Figure S6.

TMPRSS2 and ACE2 in human cells, and endogenous TMPRSS2-mediated cleavage of SARS-CoV-2 Spike, which could be blocked by camostat. This finding is consistent with work demonstrating the role of TMPRSS2 in activating Spike glycoproteins of closely related SARS-CoV and MERS-CoV (Iwata-Yoshikawa et al., 2019; Zhou et al., 2015). Our observation through immunoprecipitation experiments that TMPRSS2-ACE2 exists in complex and is potentially required for Spike cleavage has implications for developing novel therapeutics targeting the TMPRSS2-ACE2 interface to block Spike activation. Collectively, our results indicate that androgen-regulated TMPRSS2 promotes SARS-CoV-2 entry by two separate mechanisms: ACE2 interaction/cleavage, which might promote viral uptake, and SARS-2-S cleavage, which activates the S protein for membrane fusion (Hoffmann et al., 2020a, 2020c). These results have important implications for our understanding of male bias in COVID-19 severity and mortality, and provide a strong rationale for androgen deprivation or anti-androgen therapy in men with SARS-CoV-2 infection.

The evidence provided by our data and previous studies (Mikkonen et al., 2010) suggests that androgen receptor-mediated regulation of TMPRSS2 expression in non-prostatic tissues, including lung, may explain the increased susceptibility of men to COVID-19 severity and mortality. Additionally, ACE2 expression has been associated with androgen levels in men, where a lower ACE2 level was associated with older men as a consequence of lower androgen (Chen et al., 2020). Mechanistically, besides androgen, other steroid hormones (estrogen, progesterone, glucocorticoids) may also enhance TMPRSS2 and ACE2 expression in multiple tissues through binding of their respective nuclear receptors to responsive *cis* elements (ERE, PRE, GRE), which are similar to the ARE present in the gene promoter/enhancer. In addition to the regulation of TMPRSS2 and ACE2 expression, androgen could also increase the SARS-CoV-2 severity in men by modulating the immune response. Androgen is known to increase circulating neutrophils; increase secretion of IL-10, IL-2, IL-8, and TGF-β by immune cells; and decrease the antibody response to viral infections (Klein and Flanagan, 2016). It is worth noting that severe cases of COVID-19 exhibit increased neutrophils and IL-8 (Barnes et al., 2020; Takahashi et al., 2020).

Except for dexamethasone, which reduces mortality (days alive and free of mechanical ventilation) in patients in the intensive care unit by reducing inflammation (Tomazini et al., 2020), and remdesivir, which reduces disease duration by inhibiting viral replication (Goldman et al., 2020), there are currently no drugs for COVID-19. There is an urgent need for prophylactic and therapeutic interventions for patients with existing comorbidities such as cancer as they are at high risk for severe disease due to a weak immune system. Owing to an apparent male bias and assumed role of androgen in COVID-19, multiple studies have advocated androgen deprivation therapy (ADT) and anti-androgens, a mainstay of prostate cancer treatment, as potential therapeutic options in COVID-19, which could potentially provide protection against SARS-CoV-2 infection or at least reduce viral amplification (Bhowmick et al., 2020; Mjaess et al., 2020; Montopoli et al., 2020; Patel et al., 2020; Stopsack et al., 2020). Following these assumptions, various clinical trials testing ADT and anti-androgen have begun: degarelix (GnRH antagonist) NCT04397718, dutasteride (ADT) NCT04446429, bicalutamide (first-generation anti-androgen) NCT04374279, and enzalutamide (second-generation anti-androgen) NCT04475601. However, a direct link for androgen regulation of TMPRSS2 and ACE2 in tissues, including the lung, was not established until now. Additionally, camostat mesilate, the TMPRSS2 inhibitor approved for pancreatitis in Japan (Ohshio et al., 1989), is currently being investigated as a treatment for COVID-19 in several active clinical trials in the United States (NCT04353284, NCT04470544, NCT04374019), Israel (NCT04355052), and Denmark (NCT04321096). Our data showing complete block of TMPRSS2-mediated Spike activation by camostat in multiple cell line models provide further credentials for these clinical trials.

Growing evidence suggests that patients with cancer are susceptible to severe form of COVID-19 mainly due to their immunosuppressive state and co-existing medical conditions (Dai et al., 2020; Lee et al., 2020; Tang and Hu, 2020). In general, patients with metastatic cancers infected with SARS-CoV-2 have

had poorer outcomes including death, admission to the ICU, requiring mechanical ventilation, and severe symptoms (Dai et al., 2020). As the development of vaccines and anti-viral drugs against the pandemic causing SARS-CoV-2 is proceeding rapidly, camostat mesilate along with androgen regulation of TMPRSS2 and ACE2, as a means to inhibit SARS-CoV-2 cell entry (Figure 5G), and thus, the infection represents a potential strategy in treating COVID-19 in these high-risk population.

Limitations of the study

Androgen plays a vital role in the human immune response, which we did not address in this article. Research aimed at characterizing the androgen axis in context with SARS-CoV-2 infection will continue in the future.

Resource availability

Lead contact

Further information and requests for resources should be directed to and will be fulfilled by the lead contact, Irfan A. Asangani (asangani@upenn.edu).

Materials availability

This study did not generate new unique reagents.

Data and code availability

No large datasets were generated within this study. Original data can be made available from the lead contact on request.

METHODS

All methods can be found in the accompanying transparent methods supplemental file.

SUPPLEMENTAL INFORMATION

Supplemental information can be found online at https://doi.org/10.1016/j.isci.2021.102254.

ACKNOWLEDGMENTS

We thank Drs. Pöhlmann (UG, Germany), Krogan (UCLA), and Hatziioannou (RU) for SARS-CoV-2 ORFs, nano-luciferase constructs, and HEK 293T ACE2 cells. We also thank the Molecular Pathology and Imaging Core (University of Pennsylvania) for histology services and CHOP Proteomics Core for the mass spectrometry analysis. Research in I.A.A.'s laboratory is supported by NIH (1-R01 CA249210-0), Department of Defense Idea Development Award (W81XWH-17-0404), Conquer Cancer Now Award, and Sarcoma Foundation of America Research Award to I.A.A.

AUTHOR CONTRIBUTIONS

I.A.A. conceived the work. I.A.A., Q.D, and R.u.R., designed the experiments. Q.D., R.u.R., and R.R performed the experiments and acquired the data. R.N. performed bioinformatics analysis. Q.D, R.u.R., R.N., and I.A.A., interpreted the data and prepared the figures. I.A.A. wrote the manuscript with help from all the authors.

DECLARATION OF INTERESTS

The authors declare no competing interests.

Received: November 2, 2020
Revised: January 26, 2021
Accepted: February 25, 2021
Published: March 19, 2021

REFERENCES

Afar, D.E., Vivanco, I., Hubert, R.S., Kuo, J., Chen, E., Saffran, D.C., Raitano, A.B., and Jakobovits, A. (2001). Catalytic cleavage of the androgen-regulated TMPRSS2 protease results in its secretion by prostate and prostate cancer epithelia. Cancer Res. *61*, 1686–1692.

Asangani, I.A., Dommeti, V.L., Wang, X., Malik, R., Cieslik, M., Yang, R., Escara-Wilke, J., Wilder-Romans, K., Dhanireddy, S., Engelke, C., et al. (2014). Therapeutic targeting of BET bromodomain proteins in castration-resistant prostate cancer. Nature *510*, 278–282.

Barnes, B.J., Adrover, J.M., Baxter-Stoltzfus, A., Borczuk, A., Cools-Lartigue, J., Crawford, J.M., Dassler-Plenker, J., Guerci, P., Huynh, C., Knight, J.S., et al. (2020). Targeting potential drivers of COVID-19: neutrophil extracellular traps. J. Exp. Med. *217*, e20200652.

Bhowmick, N.A., Oft, J., Dorff, T., Pal, S., Agarwal, N., Figlin, R.A., Posadas, E.M., Freedland, S.J., and Gong, J. (2020). COVID-19 and androgen-targeted therapy for prostate cancer patients. Endocr. Relat. Cancer *27*, R281–R292.

de Bono, J.S., Guo, C., Gurel, B., De Marzo, A.M., Sfanos, K.S., Mani, R.S., Gil, J., Drake, C.G., and Alimonti, A. (2020). Prostate carcinogenesis: inflammatory storms. Nat. Rev. Cancer *20*, 455–469.

Cai, Y., Zhang, J., Xiao, T., Peng, H., Sterling, S.M., Walsh, R.M., Jr., Rawson, S., Rits-Volloch, S., and Chen, B. (2020). Distinct conformational states of SARS-CoV-2 spike protein. Science *369*, 1586–1592.

Chen, J., Jiang, Q., Xia, X., Liu, K., Yu, Z., Tao, W., Gong, W., and Han, J.J. (2020). Individual variation of the SARS-CoV-2 receptor ACE2 gene expression and regulation. Aging Cell *19*, e13168.

GTEx Consortium, Laboratory Data Analysis &Coordinating Center (LDACC)—Analysis Working Group, Statistical Methods groups—Analysis Working Group, Enhancing GTEx (eGTEx) groups, NIH Common Fund, NIH/NCI, NIH/NHGRI, NIH/NIMH, NIH/NIDA, Biospecimen Collection Source Site—NDRI, et al.. (2017). Genetic effects on gene expression across human tissues. Nature *550*, 204–213.

Coutard, B., Valle, C., de Lamballerie, X., Canard, B., Seidah, N.G., and Decroly, E. (2020). The spike glycoprotein of the new coronavirus 2019-nCoV contains a furin-like cleavage site absent in CoV of the same clade. Antivir. Res. *176*, 104742.

Dai, M., Liu, D., Liu, M., Zhou, F., Li, G., Chen, Z., Zhang, Z., You, H., Wu, M., Zheng, Q., et al. (2020). Patients with cancer appear more vulnerable to SARS-CoV-2: a multicenter study during the COVID-19 outbreak. Cancer Discov. *10*, 783–791.

Dubey, R.K., Oparil, S., Imthurn, B., and Jackson, E.K. (2002). Sex hormones and hypertension. Cardiovasc. Res. *53*, 688–708.

Gheblawi, M., Wang, K., Viveiros, A., Nguyen, Q., Zhong, J.C., Turner, A.J., Raizada, M.K., Grant, M.B., and Oudit, G.Y. (2020). Angiotensin-converting enzyme 2: SARS-CoV-2 receptor and regulator of the renin-angiotensin system: celebrating the 20th anniversary of the discovery of ACE2. Circ. Res. *126*, 1456–1474.

Goldman, J.D., Lye, D.C.B., Hui, D.S., Marks, K.M., Bruno, R., Montejano, R., Spinner, C.D., Galli, M., Ahn, M.Y., Nahass, R.G., et al. (2020). Remdesivir for 5 or 10 Days in patients with severe covid-19. N. Engl. J. Med. *383*, 1827–1837.

Gordon, D.E., Jang, G.M., Bouhaddou, M., Xu, J., Obernier, K., White, K.M., O'Meara, M.J., Rezelj, V.V., Guo, J.Z., Swaney, D.L., et al. (2020). A SARS-CoV-2 protein interaction map reveals targets for drug repurposing. Nature *583*, 459–468.

Hamming, I., Timens, W., Bulthuis, M.L., Lely, A.T., Navis, G., and van Goor, H. (2004). Tissue distribution of ACE2 protein, the functional receptor for SARS coronavirus. A first step in understanding SARS pathogenesis. J. Pathol. *203*, 631–637.

Han, X., Wang, C., Qin, C., Xiang, W., Fernandez-Salas, E., Yang, C.Y., Wang, M., Zhao, L., Xu, T., Chinnaswamy, K., et al. (2019). Discovery of ARD-69 as a highly potent proteolysis targeting chimera (PROTAC) degrader of androgen receptor (AR) for the treatment of prostate cancer. J. Med. Chem. *62*, 941–964.

Henry, G.H., Malewska, A., Joseph, D.B., Malladi, V.S., Lee, J., Torrealba, J., Mauck, R.J., Gahan, J.C., Raj, G.V., Roehrborn, C.G., et al. (2018). A cellular anatomy of the normal adult human prostate and prostatic urethra. Cell Rep. *25*, 3530–3542.e5.

Heurich, A., Hofmann-Winkler, H., Gierer, S., Liepold, T., Jahn, O., and Pohlmann, S. (2014). TMPRSS2 and ADAM17 cleave ACE2 differentially and only proteolysis by TMPRSS2 augments entry driven by the severe acute respiratory syndrome coronavirus spike protein. J. Virol. *88*, 1293–1307.

Hoffmann, M., Hofmann-Winkler, H., Smith, J.C., Kruger, N., Sorensen, L.K., Sogaard, O.S., Hasselstrom, J.B., Winkler, M., Hempel, T., Raich, L., et al. (2020a). Camostat mesylate inhibits SARS-CoV-2 activation by TMPRSS2-related proteases and its metabolite GBPA exerts antiviral activity. bioRxiv. https://doi.org/10.1101/2020.08.05.237651.

Hoffmann, M., Kleine-Weber, H., and Pohlmann, S. (2020b). A multibasic cleavage site in the spike protein of SARS-CoV-2 is essential for infection of human lung cells. Mol. Cell *78*, 779–784.e5.

Hoffmann, M., Kleine-Weber, H., Schroeder, S., Kruger, N., Herrler, T., Erichsen, S., Schiergens, T.S., Herrler, G., Wu, N.H., Nitsche, A., et al. (2020c). SARS-CoV-2 cell entry depends on ACE2 and TMPRSS2 and is blocked by a clinically proven protease inhibitor. Cell *181*, 271–280.e8.

Iwata-Yoshikawa, N., Okamura, T., Shimizu, Y., Hasegawa, H., Takeda, M., and Nagata, N. (2019). TMPRSS2 contributes to virus spread and immunopathology in the airways of murine models after coronavirus infection. J. Virol. *93*, e01815–18.

Kawase, M., Shirato, K., van der Hoek, L., Taguchi, F., and Matsuyama, S. (2012). Simultaneous treatment of human bronchial epithelial cells with serine and cysteine protease inhibitors prevents severe acute respiratory syndrome coronavirus entry. J. Virol. *86*, 6537–6545.

Ke, Z., Oton, J., Qu, K., Cortese, M., Zila, V., McKeane, L., Nakane, T., Zivanov, J., Neufeldt, C.J., Cerikan, B., et al. (2020). Structures and distributions of SARS-CoV-2 spike proteins on intact virions. Nature *588*, 498–502.

Klein, S.L., and Flanagan, K.L. (2016). Sex differences in immune responses. Nat. Rev. Immunol. *16*, 626–638.

Lee, L.Y.W., Cazier, J.B., Starkey, T., Briggs, S.E.W., Arnold, R., Bisht, V., Booth, S., Campton, N.A., Cheng, V.W.T., Collins, G., et al. (2020). COVID-19 prevalence and mortality in patients with cancer and the effect of primary tumour subtype and patient demographics: a prospective cohort study. Lancet Oncol. *21*, 1309–1316.

Lucas, J.M., Heinlein, C., Kim, T., Hernandez, S.A., Malik, M.S., True, L.D., Morrissey, C., Corey, E., Montgomery, B., Mostaghel, E., et al. (2014). The androgen-regulated protease TMPRSS2 activates a proteolytic cascade involving components of the tumor microenvironment and promotes prostate cancer metastasis. Cancer Discov. *4*, 1310–1325.

Mehta, P., McAuley, D.F., Brown, M., Sanchez, E., Tattersall, R.S., Manson, J.J., and Hlh Across Speciality Collaboration, U.K. (2020). COVID-19: consider cytokine storm syndromes and immunosuppression. Lancet *395*, 1033–1034.

Mikkonen, L., Pihlajamaa, P., Sahu, B., Zhang, F.P., and Janne, O.A. (2010). Androgen receptor and androgen-dependent gene expression in lung. Mol. Cell. Endocrinol. *317*, 14–24.

Millet, J.K., and Whittaker, G.R. (2015). Host cell proteases: critical determinants of coronavirus tropism and pathogenesis. Virus Res. *202*, 120–134.

Mjaess, G., Karam, A., Aoun, F., Albisinni, S., and Roumeguere, T. (2020). COVID-19 and the male susceptibility: the role of ACE2, TMPRSS2 and the androgen receptor. Prog. Urol. *30*, 484–487.

Montopoli, M., Zumerle, S., Vettor, R., Rugge, M., Zorzi, M., Catapano, C.V., Carbone, G.M., Cavalli, A., Pagano, F., Ragazzi, E., et al. (2020). Androgen-deprivation therapies for prostate cancer and risk of infection by SARS-CoV-2: a population-based study (N = 4532). Ann. Oncol. *31*, 1040–1045.

Montoro, D.T., Haber, A.L., Biton, M., Vinarsky, V., Lin, B., Birket, S.E., Yuan, F., Chen, S., Leung, H.M., Villoria, J., et al. (2018). A revised airway epithelial hierarchy includes CFTR-expressing ionocytes. Nature *560*, 319–324.

Moore, J.B., and June, C.H. (2020). Cytokine release syndrome in severe COVID-19. Science *368*, 473–474.

Morens, D.M., and Fauci, A.S. (2020). Emerging pandemic diseases: how we got to COVID-19. Cell *182*, 1077–1092.

Muus, C., Luecken, M.D., Eraslan, G., Waghray, A., Heimberg, G., Sikkema, L., Kobayashi, Y., Vaishnav, E.D., Subramanian, A., Smilie, C., et al. (2020). Integrated analyses of single-cell atlases reveal age, gender, and smoking status associations with cell type-specific expression of

mediators of SARS-CoV-2 viral entry and highlights inflammatory programs in putative target cells. bioRxiv, 2020.2004.2019.049254.

Nersisyan, S., Shkurnikov, M., Turchinovich, A., Knyazev, E., and Tonevitsky, A. (2020). Integrative analysis of miRNA and mRNA sequencing data reveals potential regulatory mechanisms of ACE2 and TMPRSS2. PLoS One *15*, e0235987.

Ohshio, G., Saluja, A.K., Leli, U., Sengupta, A., and Steer, M.L. (1989). Esterase inhibitors prevent lysosomal enzyme redistribution in two noninvasive models of experimental pancreatitis. Gastroenterology *96*, 853–859.

Patel, V.G., Zhong, X., Liaw, B., Tremblay, D., Tsao, C.K., Galsky, M.D., and Oh, W.K. (2020). Does androgen deprivation therapy protect against severe complications from COVID-19? Ann. Oncol. *31*, 1419–1420.

Pihlajamaa, P., Sahu, B., Lyly, L., Aittomaki, V., Hautaniemi, S., and Janne, O.A. (2014). Tissue-specific pioneer factors associate with androgen receptor cistromes and transcription programs. EMBO J. *33*, 312–326.

Rasool, R.U., Natesan, R., Deng, Q., Aras, S., Lal, P., Sander Effron, S., Mitchell-Velasquez, E., Posimo, J.M., Carskadon, S., Baca, S.C., et al. (2019). CDK7 inhibition suppresses castration-resistant prostate cancer through MED1 inactivation. Cancer Discov. *9*, 1538–1555.

Shang, J., Wan, Y., Luo, C., Ye, G., Geng, Q., Auerbach, A., and Li, F. (2020). Cell entry mechanisms of SARS-CoV-2. Proc. Natl. Acad. Sci. U S A *117*, 11727–11734.

Shulla, A., Heald-Sargent, T., Subramanya, G., Zhao, J., Perlman, S., and Gallagher, T. (2011). A transmembrane serine protease is linked to the severe acute respiratory syndrome coronavirus receptor and activates virus entry. J. Virol. *85*, 873–882.

Song, H., Seddighzadeh, B., Cooperberg, M.R., and Huang, F.W. (2020). Expression of ACE2, the SARS-CoV-2 receptor, and TMPRSS2 in prostate epithelial cells. Eur. Urol. *78*, 296–298.

Stopsack, K.H., Mucci, L.A., Antonarakis, E.S., Nelson, P.S., and Kantoff, P.W. (2020). TMPRSS2 and COVID-19: serendipity or opportunity for intervention? Cancer Discov. *10*, 779–782.

Takahashi, T., Ellingson, M.K., Wong, P., Israelow, B., Lucas, C., Klein, J., Silva, J., Mao, T., Oh, J.E., Tokuyama, M., et al. (2020). Sex differences in immune responses that underlie COVID-19 disease outcomes. Nature *588*, 315–320.

Tang, L.V., and Hu, Y. (2020). Poor clinical outcomes for patients with cancer during the COVID-19 pandemic. Lancet Oncol. *21*, 862–864.

Tomazini, B.M., Maia, I.S., Cavalcanti, A.B., Berwanger, O., Rosa, R.G., Veiga, V.C., Avezum, A., Lopes, R.D., Bueno, F.R., Silva, M., et al. (2020). Effect of dexamethasone on days alive and ventilator-free in patients with moderate or severe acute respiratory distress syndrome and COVID-19: the CoDEX randomized clinical trial. JAMA *324*, 1307–1316.

Tomlins, S.A., Rhodes, D.R., Perner, S., Dhanasekaran, S.M., Mehra, R., Sun, X.W., Varambally, S., Cao, X., Tchinda, J., Kuefer, R., et al. (2005). Recurrent fusion of TMPRSS2 and ETS transcription factor genes in prostate cancer. Science *310*, 644–648.

Turonova, B., Sikora, M., Schurmann, C., Hagen, W.J.H., Welsch, S., Blanc, F.E.C., von Bulow, S., Gecht, M., Bagola, K., Horner, C., et al. (2020). In situ structural analysis of SARS-CoV-2 spike reveals flexibility mediated by three hinges. Science *370*, 203–208.

Vabret, N., Britton, G.J., Gruber, C., Hegde, S., Kim, J., Kuksin, M., Levantovsky, R., Malle, L., Moreira, A., Park, M.D., et al. (2020). Immunology of COVID-19: current state of the science. Immunity *52*, 910–941.

La Vignera, S., Cannarella, R., Condorelli, R.A., Torre, F., Aversa, A., and Calogero, A.E. (2020). Sex-specific SARS-CoV-2 mortality: among hormone-modulated ACE2 expression, risk of venous thromboembolism and hypovitaminosis D. Int. J. Mol. Sci. *21*, 2948.

Wadman, M. (2020). Sex hormones signal why virus hits men harder. Science *368*, 1038–1039.

Walls, A.C., Tortorici, M.A., Snijder, J., Xiong, X., Bosch, B.J., Rey, F.A., and Veesler, D. (2017). Tectonic conformational changes of a coronavirus spike glycoprotein promote membrane fusion. Proc. Natl. Acad. Sci. U S A *114*, 11157–11162.

Walls, A.C., Park, Y.J., Tortorici, M.A., Wall, A., McGuire, A.T., and Veesler, D. (2020). Structure, function, and antigenicity of the SARS-CoV-2 spike glycoprotein. Cell *181*, 281–292 e286.

Wang, C., Horby, P.W., Hayden, F.G., and Gao, G.F. (2020). A novel coronavirus outbreak of global health concern. Lancet *395*, 470–473.

Williamson, E.J., Walker, A.J., Bhaskaran, K., Bacon, S., Bates, C., Morton, C.E., Curtis, H.J., Mehrkar, A., Evans, D., Inglesby, P., et al. (2020). Factors associated with COVID-19-related death using OpenSAFELY. Nature *584*, 430–436.

Zhang, X., Tan, Y., Ling, Y., Lu, G., Liu, F., Yi, Z., Jia, X., Wu, M., Shi, B., Xu, S., et al. (2020). Viral and host factors related to the clinical outcome of COVID-19. Nature *583*, 437–440.

Zhou, Y., Vedantham, P., Lu, K., Agudelo, J., Carrion, R., Jr., Nunneley, J.W., Barnard, D., Pohlmann, S., McKerrow, J.H., Renslo, A.R., et al. (2015). Protease inhibitors targeting coronavirus and filovirus entry. Antivir. Res *116*, 76–84.

Ziegler, C.G.K., Allon, S.J., Nyquist, S.K., Mbano, I.M., Miao, V.N., Tzouanas, C.N., Cao, Y., Yousif, A.S., Bals, J., Hauser, B.M., et al. (2020). SARS-CoV-2 receptor ACE2 is an interferon-stimulated gene in human airway epithelial cells and is detected in specific cell subsets across tissues. Cell *181*, 1016–1035 e1019.

iScience, Volume *24*

Supplemental information

Targeting androgen regulation of TMPRSS2 and ACE2 as a therapeutic strategy to combat COVID-19

Qu Deng, Reyaz ur Rasool, Ronnie M. Russell, Ramakrishnan Natesan, and Irfan A. Asangani

Supplementary Figure 1

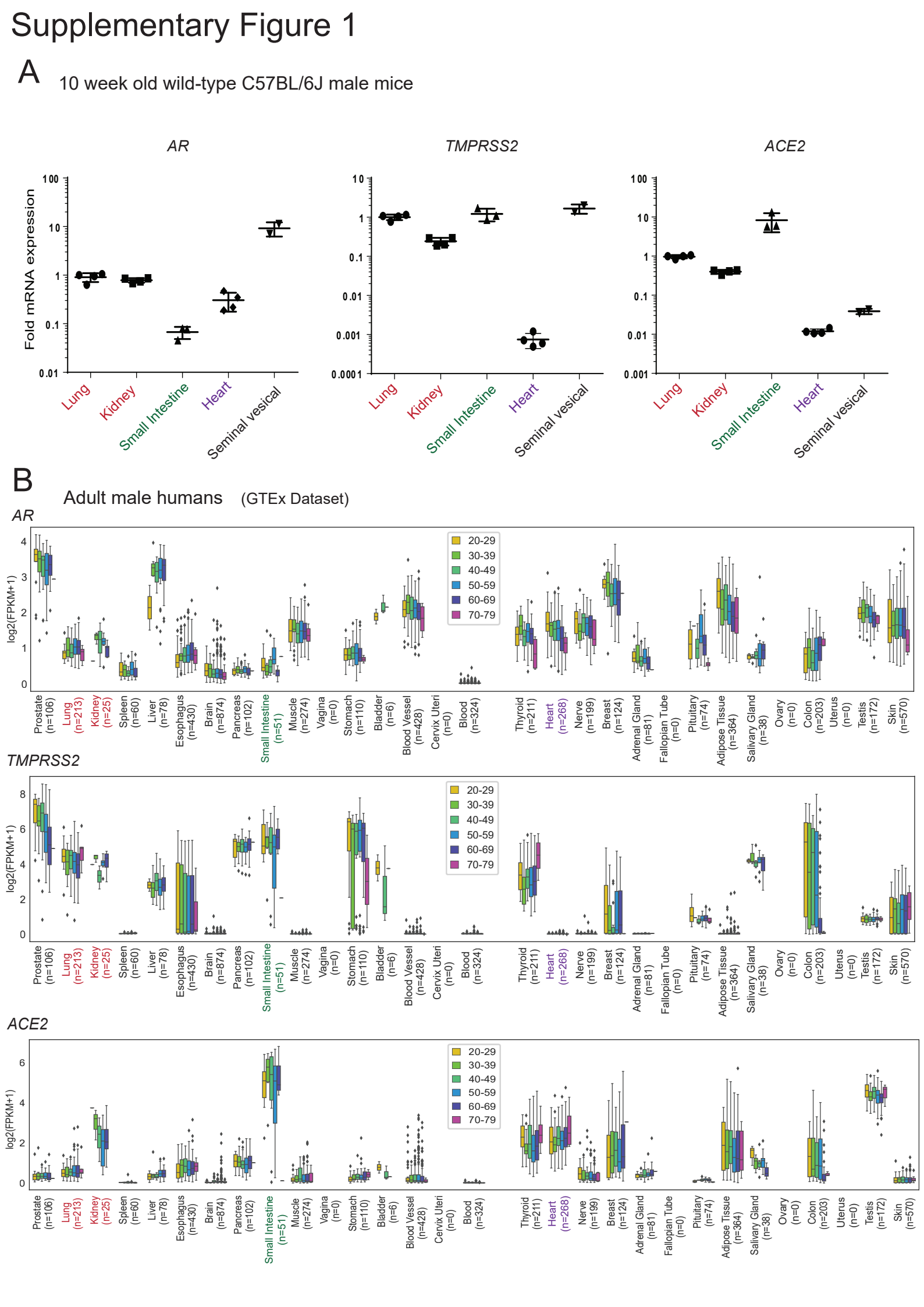

Supplementary Figure 1. Expression of AR, ACE2 and TMPRSS2 in mice and human male. **(A)** Expression of AR, ACE2 and TMPRSS2 in various organs in adult male mice. qRT-PCR analysis for AR in the indicated organs from mock castrated male mice. **(B)** GTEx data showing the AR, TMPRSS2 and ACE2 mRNA expression in various organs in human male. Related to Figure. 1.

Supplementary Figure 2

A

IHC negative controls

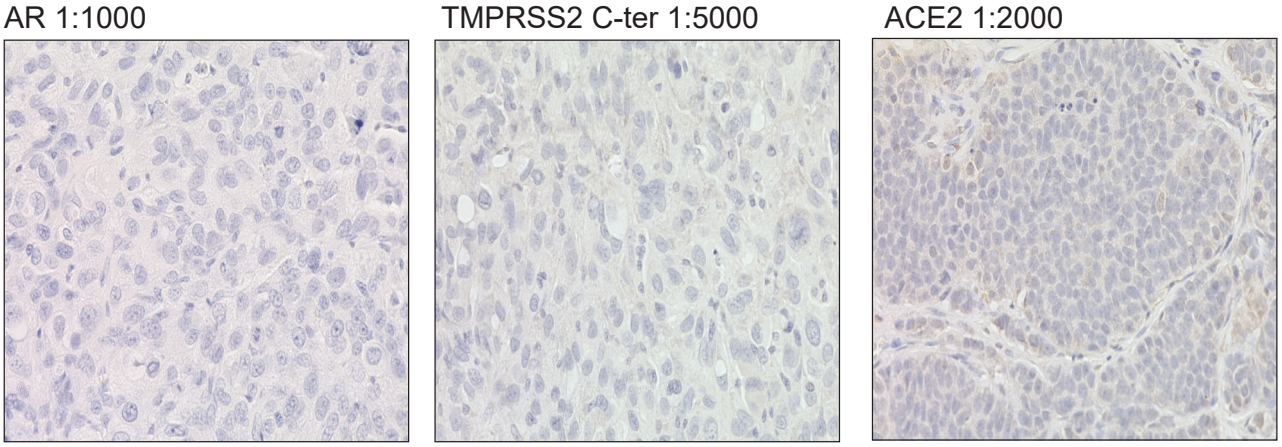

B

Seminal vesicles

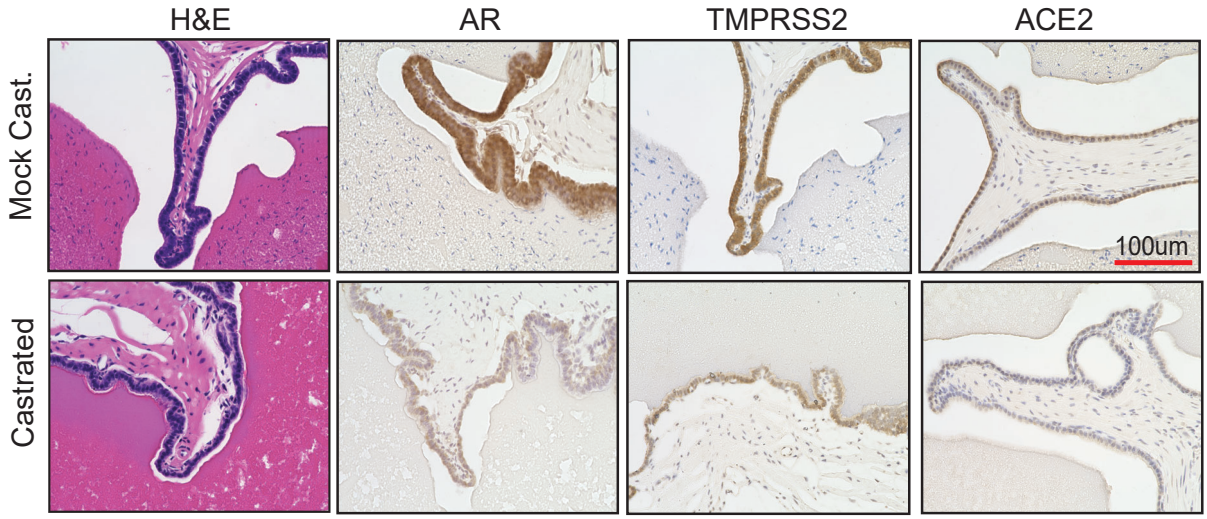

C

Lungs

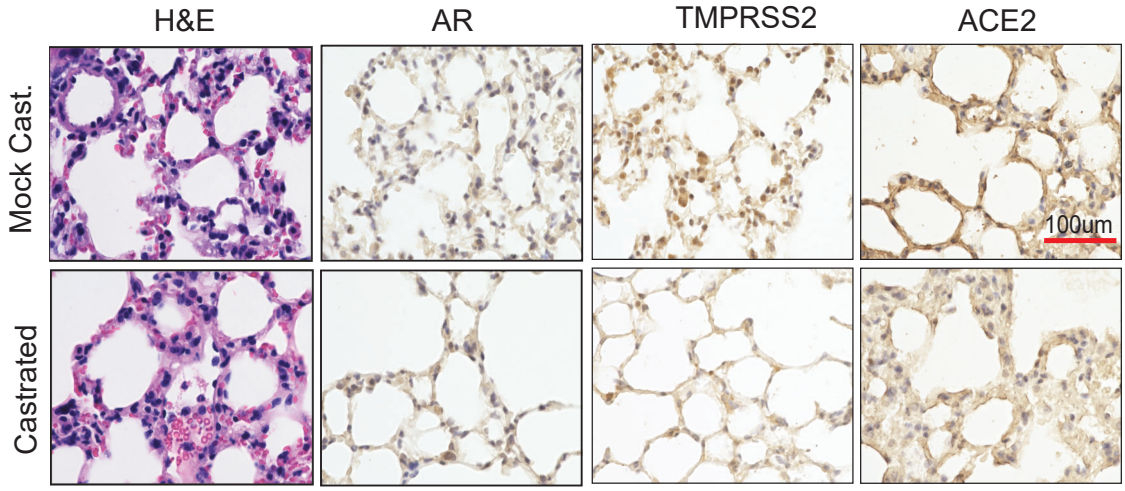

Supplementary Figure 2. Immunohistochemistry staining for AR, TMPRSS2 and ACE2 in mice and human cells. (A) Negative control for immunohistochemistry staining data presented in Figure 1D and 1E. Immunohistochemistry with AR, TMRPSS2 and ACE2 antibody at the indicated dilution was performed on AR and TMPRSS2 negative DU145 xenograft tissue section, and ACE2 negative VCaP xenograft tissue section. **(B)** Immunohistochemistry analysis of the indicated target protein in the seminal vesicles from mock and castrated males. Note the reduced AR, TMPRSS2, and ACE2 staining in the castrated group compared to mock. **(C)** Higher magnification images for the staining of lung tissues shown in Fig. 1E. Note the reduced TMPRSS2 and ACE2 staining intensity in the castrated group. Related to Figure. 1.

Supplementary Figure 3

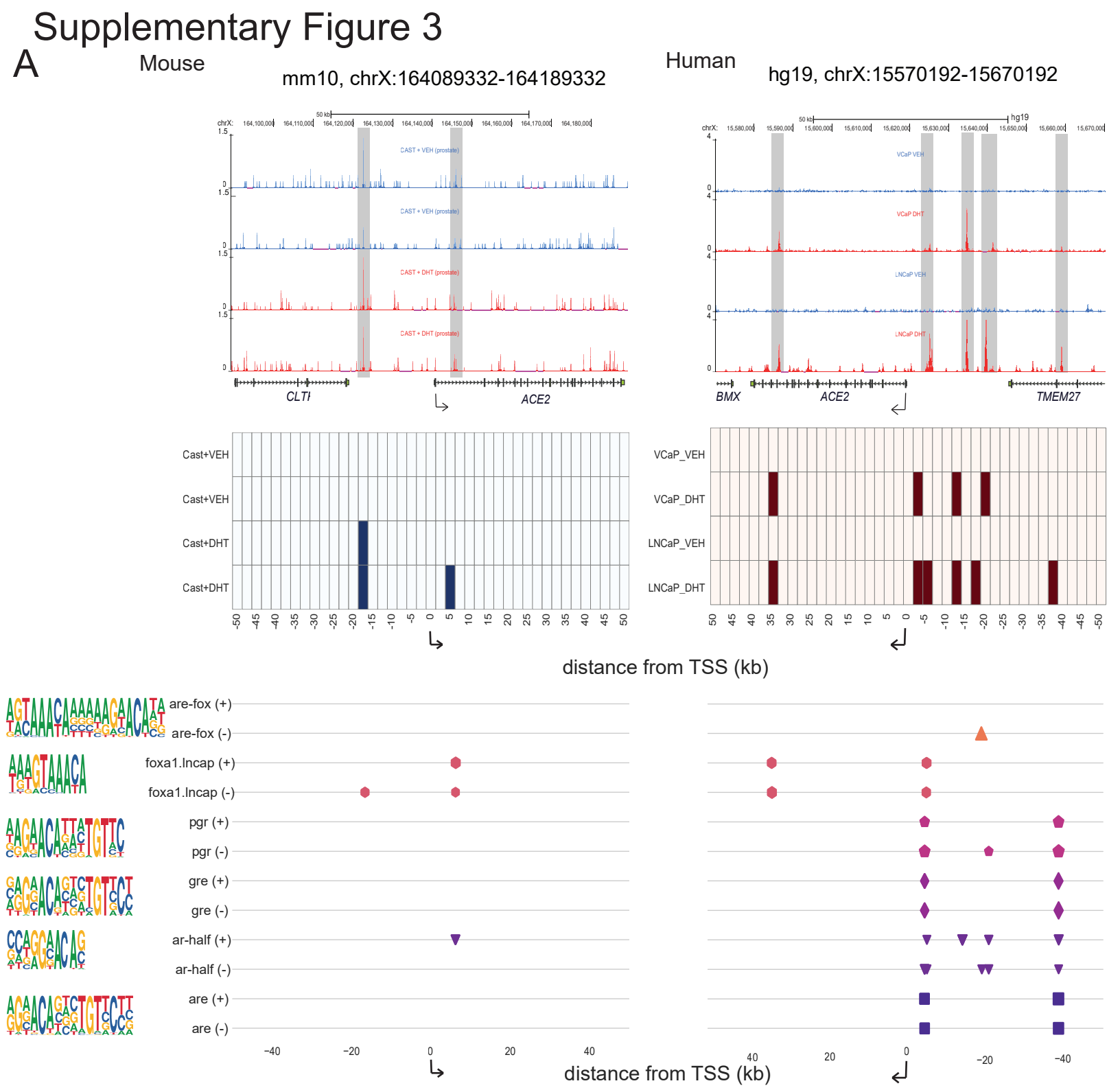

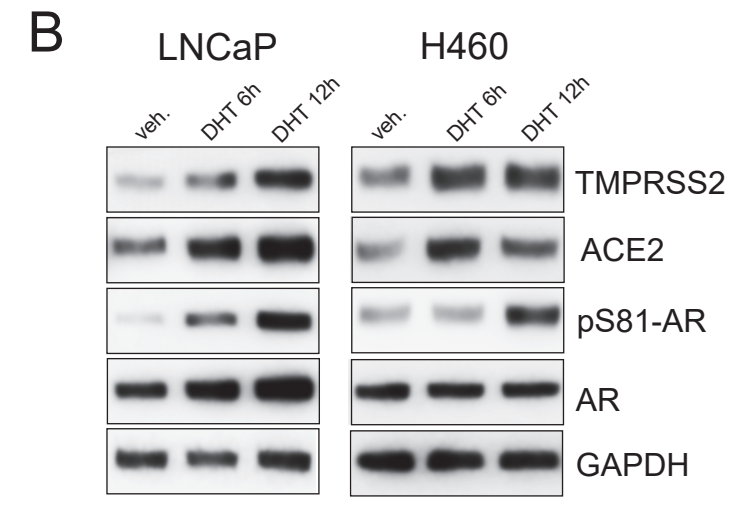

Supplementary Figure 3. *TMPRSS2* and *ACE2* loci displays enhanced AR-binding upon testosterone stimulation. (A) Shown are AR ChIP-seq tracks in vehicle and testosterone treated conditions, their enrichment profile, and the locations of six canonical AR motifs, in the region 50 kb up- and down-stream of *Ace2* (left panel) and *ACE2* (right panel). The shown tracks are from the publicly available datasets GSE47192 (castrated mouse prostate) and GSE125245 (VCaP and LNCaP lines previously published from our laboratory). All dataset were analyzed as described in the methods section. **(B)** Increase in TMPRSS2 and ACE2 protein upon DHT stimulation. LNCaP and H460 cells were grown in CSS media for 48h followed by stimulation with 10 nM for 6h and 12h. Total lysates prepared were used for immunoblotting with indicated antibodies. GAPDH was used loading control. Related to Figure. 2.

Supplementary Figure 4

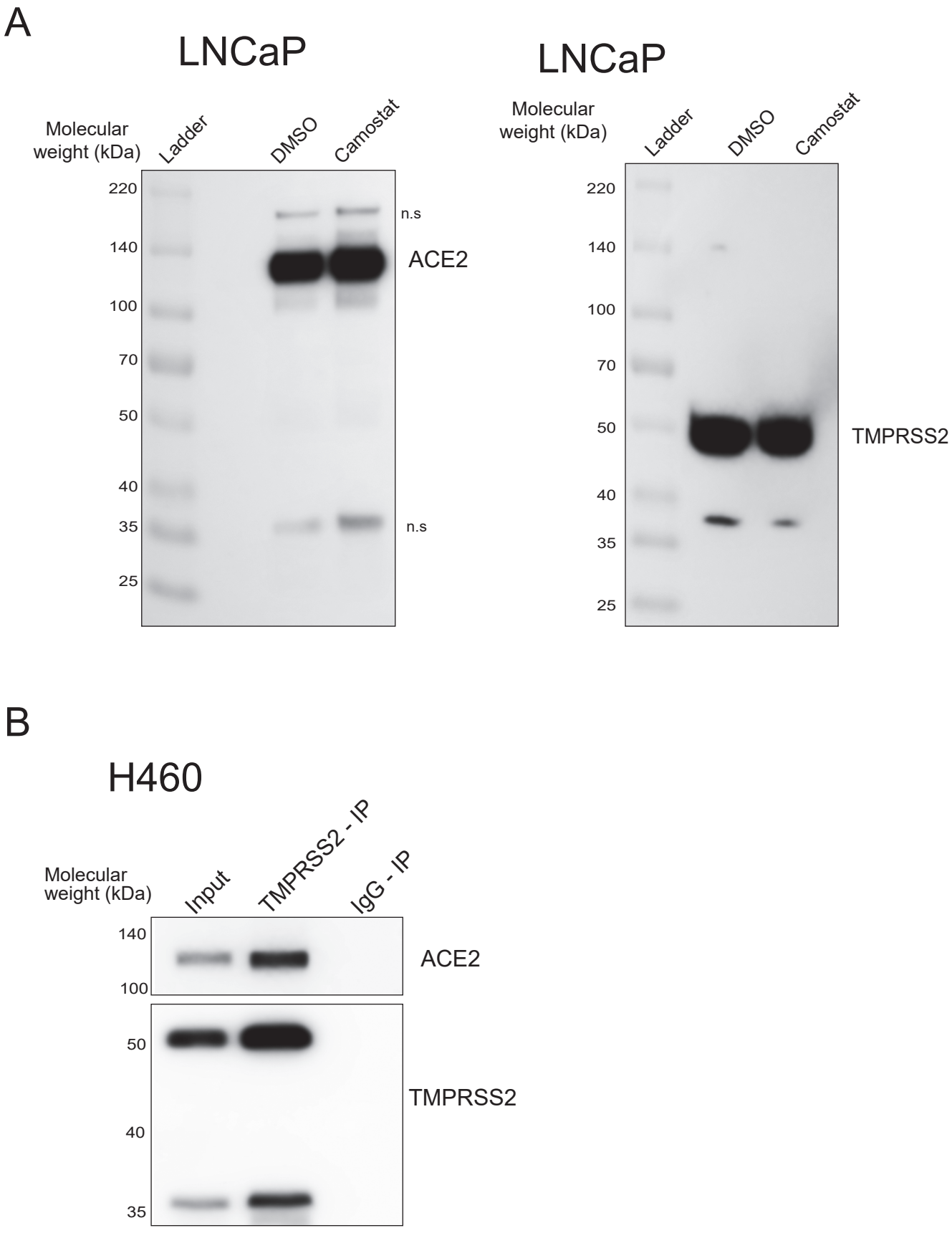

Supplementary Figure 4. Effect of Camostat on ACE2, and interaction between ACE2-TMPRSS2 in H460 cells. (A) Camostat does not affect TMRPSS2 or ACE2 levels. Immunoblot showing TMPRSS2and ACE2 levels in LNCaP cells treated with DMSO or Camostat (250 uM) for 24h. Protein molecular weight ladder used to determine the exact size of the target protein. **(B)** TMPRSS2 and ACE2 physically interacts in H460 cells. Immunoprecipitation using C-terminal TMPRSS2 antibody with H460 protein extracts, followed by immunoblotting with ACE2 and TMRPSS2 antibody. IgG pulldown served as a negative control; input was 10%. Related to Figure. 3.

Supplementary Figure 5

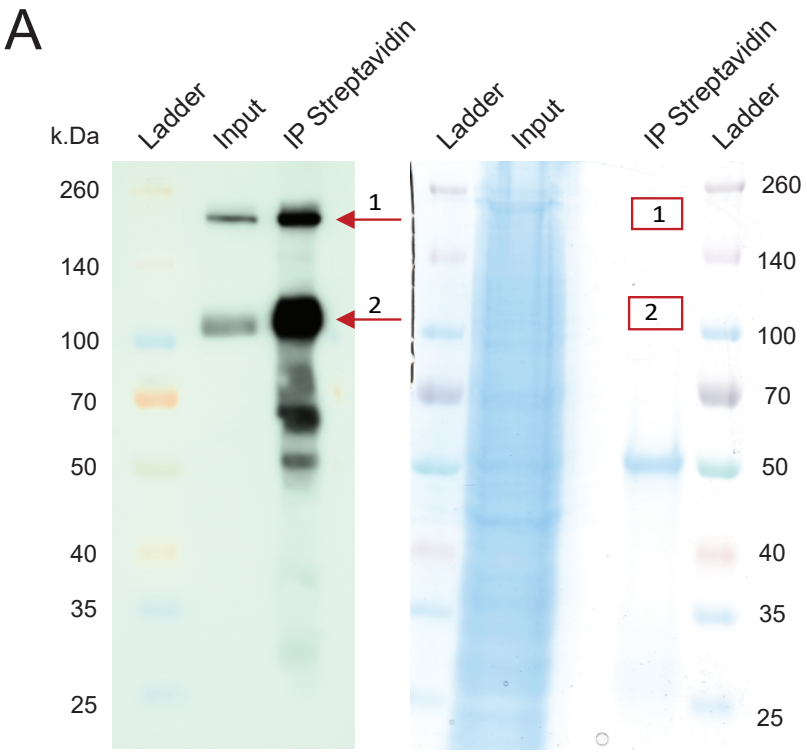

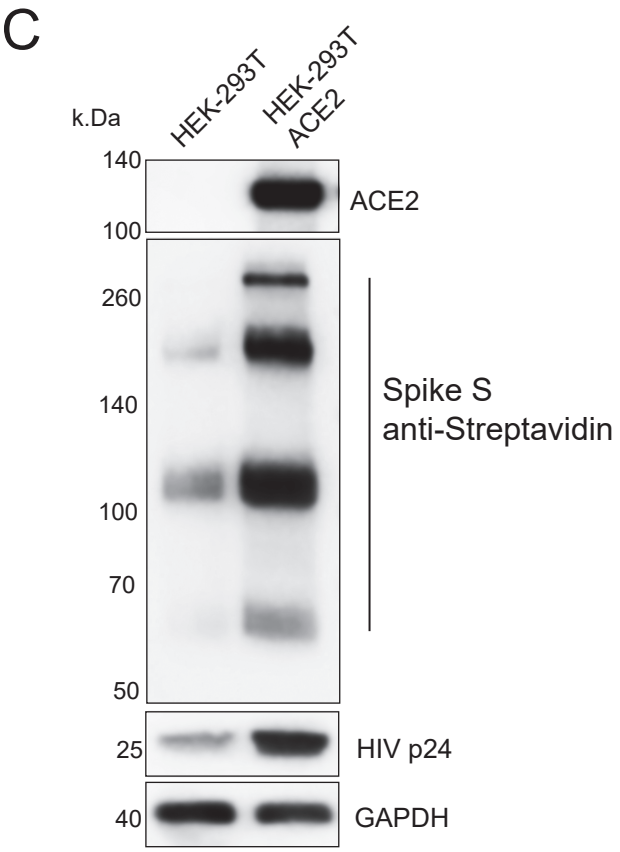

B

Band 1

P0DTC2 (100%), 141,180.7 Da
Spike glycoprotein OS=Severe acute respiratory syndrome coronavirus 2 OX=2697049 GN=S PE=1 SV=1
52 exclusive unique peptides, 78 exclusive unique spectra, 210 total spectra, 654/1273 amino acids (51% coverage)

MFVFLVLLPL VSSQCVNLTT RTQLPPAYTN SFTRGVYYPD KVFRSSVLHS TQDLFLPFFS NVTWFHAIHV SGTNGTKRFD
NPVLPFNDGV YFASTEKSNI IRGWIFGTTL DSKTQSLLIV NNATNVVIKV CEFQFCNDPF LGVYYHKNNK SWMESEFRVY
SSANNCTFEY VSQPFLMDLE GKQGNFKNLR EFVFKNIDGY FKIYSKHTPI NLVRDLPQGF SALEPLVDLP IGINITRFQT
LLALHRSYLT PGDSSSGWTA GAAAYYVGYL QPRTFLLKYN ENGTITDAVD CALDPLSETK CTLKSFTVEK GIYQTSNFRV
QPTESIVRFP NITNLCPFGE VFNATRFASV YAWNRKRISN CVADYSVLYN SASFSTFKCY GVSPTKLNDL CFTNVYADSF
VIRGDEVRQI APGQTGKIAD YNYKLPDDFT GCVIAWNSNN LDSKVGGNYN YLYRLFRKSN LKPFERDIST EIYQAGSTPC
NGVEGFNCYF PLQSYGFQPT NGVGYQPYRV VVLSFELLHA PATVCGPKKS TNLVKNKCVN FNFNGLTGTG VLTESNKKFL
PFQQFGRDIA DTTDAVRDPQ TLEILDITPC SFGGVSVITP GTNTSNQVAV LYQDVNCTEV PVAIHADQLT PTWRVYSTGS
NVFQTRAGCL IGAEHVNNSY ECDIPIGAGI CASYQTQTNS PRRARSVASQ SIIAYTMSLG AENSVAYSNN SIAIPTNFTI
SVTTEILPVS MTKTSVDCTM YICGDSTECS NLLLQYGSFC TQLNRALTGI AVEQDKNTQE VFAQVKQIYK TPPIKDFGGF
NFSQILPDPS KPSKRSFIED LLFNKVTLAD AGFIKQYGDC LGDIAARDLI CAQKFNGLTV LPPLLTDEMI AQYTSALLAG
TITSGWTFGA GAALQIPFAM QMAYRFNGIG VTQNVLYENQ KLIANQFNSA IGKIQDSLSS TASALGKLQD VVNQNAQALN
TLVKQLSSNF GAISSVLNDI LSRLDKVEAE VQIDRLITGR LQSLQTYVTQ QLIRAAEIRA SANLAATKMS ECVLGQSKRV
DFCGKGYHLM SFPQSAPHGV VFLHVTYVPA QEKNFTTAPA ICHDGKAHFP REGVFVSNGT HWFVTQRNFY EPQIITTDNT
FVSGNCDVVI GIVNNTVYDP LQPELDSFKE ELDKYFKNHT SPDVDLGDIS GINASVVNIQ KEIDRLNEVA KNLNESLIDL
QELGKYEQYI KWPWYIWLGF IAGLIAIVMV TIMLCCMTSC CSCLKGCCSC GSCCKFDEDD SEPVLKGVKL HYT

Band 2

P0DTC2 (100%), 141,180.7 Da
Spike glycoprotein OS=Severe acute respiratory syndrome coronavirus 2 OX=2697049 GN=S PE=1 SV=1
57 exclusive unique peptides, 82 exclusive unique spectra, 224 total spectra, 682/1273 amino acids (54% coverage)

MFVFLVLLPL VSSQCVNLTT RTQLPPAYTN SFTRGVYYPD KVFRSSVLHS TQDLFLPFFS NVTWFHAIHV SGTNGTKRFD
NPVLPFNDGV YFASTEKSNI IRGWIFGTTL DSKTQSLLIV NNATNVVIKV CEFQFCNDPF LGVYYHKNNK SWMESEFRVY
SSANNCTFEY VSQPFLMDLE GKQGNFKNLR EFVFKNIDGY FKIYSKHTPI NLVRDLPQGF SALEPLVDLP IGINITRFQT
LLALHRSYLT PGDSSSGWTA GAAAYYVGYL QPRTFLLKYN ENGTITDAVD CALDPLSETK CTLKSFTVEK GIYQTSNFRV
QPTESIVRFP NITNLCPFGE VFNATRFASV YAWNRKRISN CVADYSVLYN SASFSTFKCY GVSPTKLNDL CFTNVYADSF
VIRGDEVRQI APGQTGKIAD YNYKLPDDFT GCVIAWNSNN LDSKVGGNYN YLYRLFRKSN LKPFERDIST EIYQAGSTPC
NGVEGFNCYF PLQSYGFQPT NGVGYQPYRV VVLSFELLHA PATVCGPKKS TNLVKNKCVN FNFNGLTGTG VLTESNKKFL
PFQQFGRDIA DTTDAVRDPQ TLEILDITPC SFGGVSVITP GTNTSNQVAV LYQDVNCTEV PVAIHADQLT PTWRVYSTGS
NVFQTRAGCL IGAEHVNNSY ECDIPIGAGI CASYQTQTNS PRRARSVASQ SIIAYTMSLG AENSVAYSNN SIAIPTNFTI
SVTTEILPVS MTKTSVDCTM YICGDSTECS NLLLQYGSFC TQLNRALTGI AVEQDKNTQE VFAQVKQIYK TPPIKDFGGF
NFSQILPDPS KPSKRSFIED LLFNKVTLAD AGFIKQYGDC LGDIAARDLI CAQKFNGLTV LPPLLTDEMI AQYTSALLAG
TITSGWTFGA GAALQIPFAM QMAYRFNGIG VTQNVLYENQ KLIANQFNSA IGKIQDSLSS TASALGKLQD VVNQNAQALN
TLVKQLSSNF GAISSVLNDI LSRLDKVEAE VQIDRLITGR LQSLQTYVTQ QLIRAAEIRA SANLAATKMS ECVLGQSKRV
DFCGKGYHLM SFPQSAPHGV VFLHVTYVPA QEKNFTTAPA ICHDGKAHFP REGVFVSNGT HWFVTQRNFY EPQIITTDNT
FVSGNCDVVI GIVNNTVYDP LQPELDSFKE ELDKYFKNHT SPDVDLGDIS GINASVVNIQ KEIDRLNEVA KNLNESLIDL
QELGKYEQYI KWPWYIWLGF IAGLIAIVMV TIMLCCMTSC CSCLKGCCSC GSCCKFDEDD SEPVLKGVKL HYT

Supplementary Figure 5. Mass spectrometry analysis of pseudotype SARS-2-S proteins. (A), *Left,* Proteins extracted from purified pseudotype SARS-2-S virus were subjected to immunoprecipitation with streptavidin antibody followed by immunoblotting. Arrow indicates two prominent bands analyzed for sequencing. *Right,* SDS-PAGE and Coomassie stain gel with the streptavidin immunoprecipitated eluates. Box indicates the excised regions of gel used for protein extraction for mass spectrometry. **(B)** SARS-2-S protein sequence with peptide coverage highlighted in yellow for band 1 and band 2. Total spectra and unique peptides for both the bands are indicated on the top. **(C)** Pseudotype SARS-CoV-2 Spike requires ACE2 for cell entry. HEK 293T and HEK 293T ACE2 overexpressing cells were infected with pseudotype HIV bearing SARS-CoV-2 Spike via spinoculation for 1h. Next, 4h post-spinoculation recovery total lysates were prepared and used for immunoblotting with the indicated antibody. Note the increased signal for different forms of Spike proteins and HIV p24 in the ACE2 expressing cells. GAPDH was used as a loading control. Related to Figure. 4.

Supplementary Figure 6

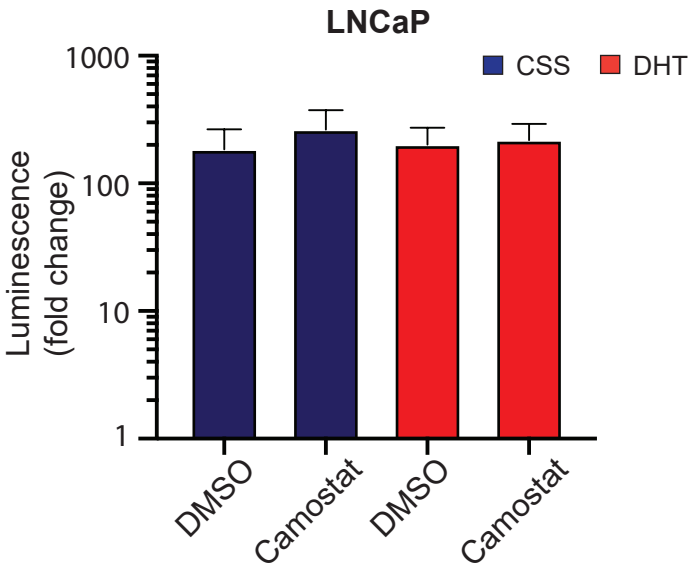

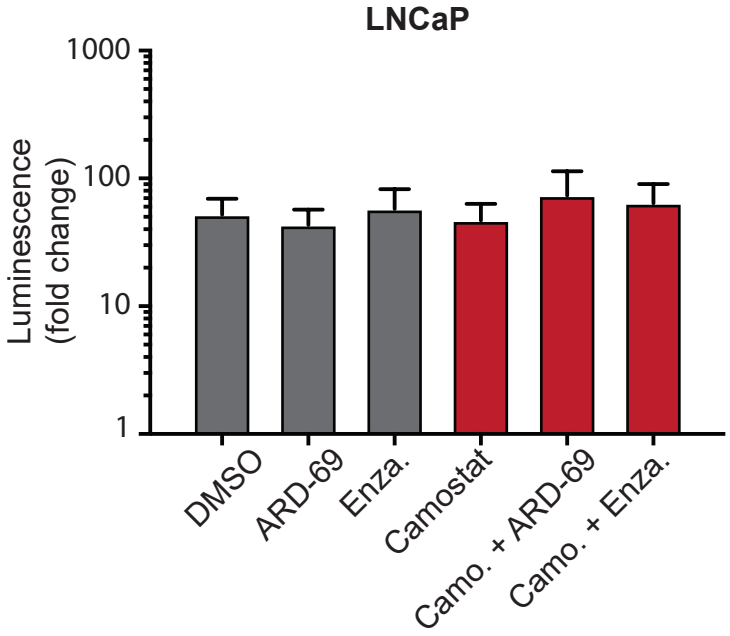

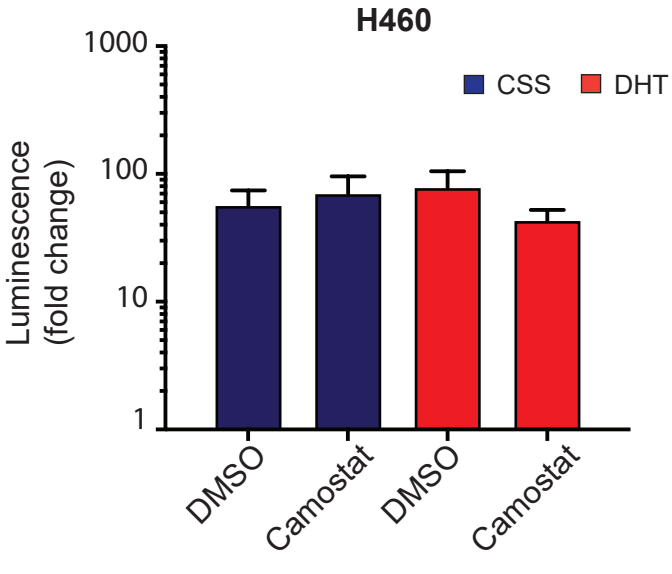

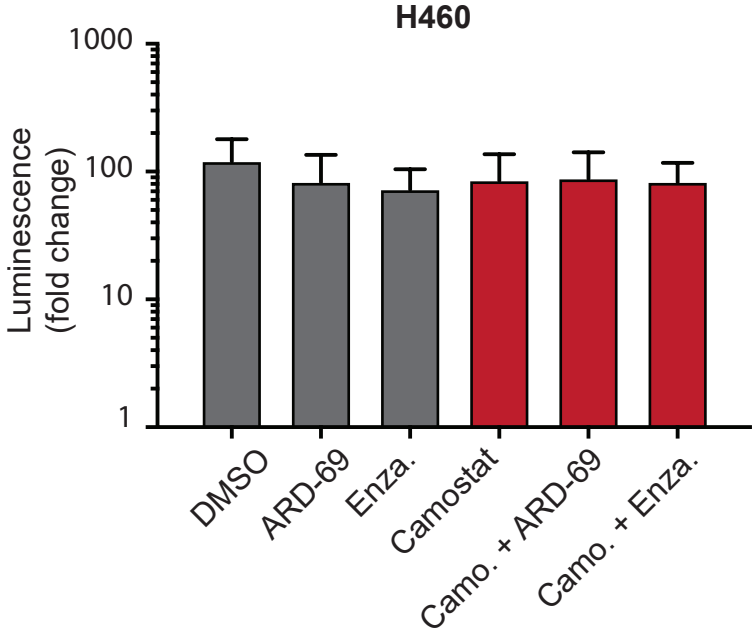

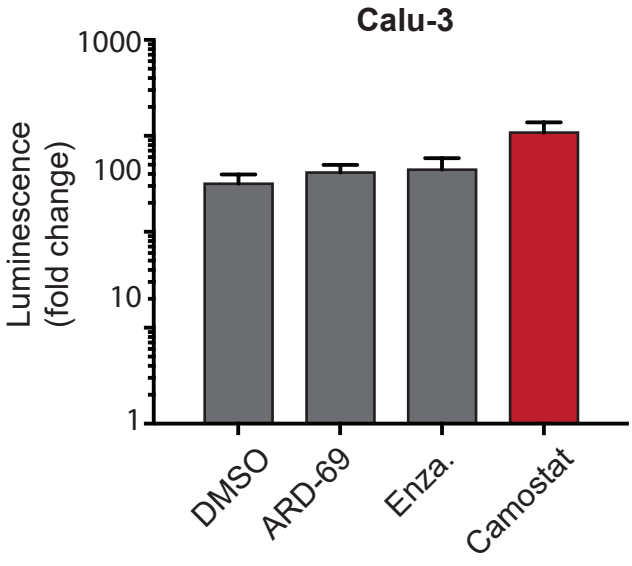

Supplementary Figure 6. VSV-G pseudotype entry is not affected by ADT, anti-androgens or Camostat treatment. As in figure 5 with VSV-G pseudotype entry in LNCaP, H460 and Calu-3 cells under different conditions as in Figure 5. Briefly, LNCaP and H460 cells grown in androgen-deprived serum containing media for three days were pretreated with DMSO, DHT (10 nM) or Camostat (300 μM) for 1h followed by inoculation with VSV-G pseudovirus. 24h post-inoculation, the pseudovirus entry efficiency was measured by means of nano-luciferase signal accompanying entry. LNCaP and H460 cells grown in complete media was pretreated with enzalutamide (10 μM) or ARD-69 (500 nM) alone, or in combination with Camostat (300 μM) for 1h followed by inoculation with VSV-G pseudovirus. 24h post-inoculation reporter activity was measured. Calu-3 cell were pretreated with enzalutamide**,** ARD-69 or Camostat followed by VSV-G pseudovirus inoculation. 24h later reporter signal characterizes the pseudovirus entry efficiency. Error bar indicates SEM (n =5). Related to Figure. 5.

Transparent Methods

Mouse castration experiment

In vivo mouse studies were performed following protocols approved by the Institutional Animal Care and Use Committee at the University of Pennsylvania and in compliance with all regulatory standards. C57BL/6J mice were procured from Jackson Laboratory (000664) and breed in house. Eight-to-nine-week-old C57BL/6J male mice were randomized into two groups; one group underwent surgical castration, while the other group had a mock surgery. 8 days post-castration, mice were euthanized, and major organs were harvested for RNA, protein, and immunohistochemistry analysis. The female mice were used as control.

Immunohistochemistry

Tissues were fixed in 4% of formaldehyde for 48h, and paraffin embedded through Molecular Pathology and Imaging Core at UPENN. Paraffin embedded sections from the tissue of mock castrated male, castrated male and female mice were deparaffinized with 3 changes of xylene for 5 min each. Slides were then rehydrated in 100% alcohol for 10min, 95% alcohol 10min for 2 changes, 70% alcohol and distilled water for 10min each. Slides were subjected to citrate based (pH 6.0) antigen retrieval (Vector, H-3300) at 95°C for 30mins and followed by blocking endogenous peroxidase activity with 3% H_2O_2 for 5min. After three times of 5 min TBST washing, slides were with blocking buffer (1.25% of goat serum) at room temperature for one hour. Slides were applied with diluted primary antibody and incubated in a humidified chamber at 4°C overnight. After three times of 10min TBST washing, slides were incubated with secondary antibody (Vector, PK-4001 and R&D, CTS008) for 30min at room temperature. After three times of 10min TBST washing, the color of the antibody staining was revealed by peroxidase-based detection (R&D, CTS008) and the sections were counterstained with hematoxylin (Millipore Sigma, MHS1). Representative photographs were taken on a Keyence BZ-X Series All-in-one Fluorescence Microscope with a 20x and 40 x objectives. Images were assessed and quantified with ImageJ.

ChIP-seq analysis

Publically available castrated mouse prostate AR ChIP-seq (Chromatin Immunoprecipitation followed by sequencing) data submitted to Gene Expression Omnibus (GSE47192) was

downloaded as raw fastq files, quality checked using FASTQC (www.bioinformatics.babraham.ac.uk/projects/fastqc) and aligned to the GRCm38 (release 19) genome using the STAR v2.7.3a aligner with default settings. PCR duplicate reads in the aligned bam files were removed using samtools, bam files were converted to CPM normalized bigwig tracks using deeptools, and viewed using the Integrated Genomics Viewer or the UCSC genome browser. Single-end reads were extended up to the fragment length (200 bp) along the read direction. ChIP-sequencing data for human prostate lines VCaP and LNCaP from our lab and previously submitted to GEO (GSE125245) were analyzed as described and aligned to GRCh37 (release 10) reference genome.

ChIP-Enrichment analysis

AR enrichment peaks in both human and mouse ChIP-seq data were computed using MACS2(Zhang et al., 2008), with default settings. Regions found to ubiquitously enriched across a number of next-generation sequencing experiments, also known as the blacklisted peaks (https://sites.google.com/site/anshulkundaje/projects/blacklists), were excluded in all subsequent analysis. Heatmaps of various ChIP-enriched regions (2500 kbp spatial resolution, p-value<0.05) were assembled using in-house python scripts.

Motif enrichment analysis

The presence and enrichment of various AR-binding motifs within AR-enriched regions 50 kb up- and down-stream of *ACE2*/*Ace2* were determined using HOMER (Heinz et al., 2010). Briefly, position weight matrices for well-established AR motifs, namely **are, are-fox, ar-half, foxa1.lncap, gre,** and **pgr** (all sourced from the HOMER package), were supplied to findGenomeMotifs.pl using the -find option. The resulting enrichment data was plotted as a scatter plot as shown in Supplementary Fig. 3A using in-house python scripts.

Gene expression analysis

The transcriptomic dataset from Genotype-Tissue Expression (GTEx V6p, n = 11401) and associated metadata (Consortium et al., 2017) were downloaded from GTEx website and analyzed using in-house scripts. The metadata was incorporated into the expression matrix to construct sex,

age, and organ-specific cohorts for *AR, ACE2* and *TMPRSS2* as shown in Supplementary Figure 1B.

RNA extraction and quantitative RT-PCR

Total RNA was isolated from cells and tissue using miRNeasy Mini Kit (Qiagen, 74106), and cDNA was synthesized from 1µg total RNA using SuperScriptIV (Life Technologies,18090200). qRT-PCR was performed in triplicates using Fast SYBR Master Mix (Life Technologies, 4385617), and analyzed on QuantStudio3 (Applied Biosystems, USA). The target mRNA expression was quantified using ΔΔCt method, as normalized to GAPDH transcript levels. Primers were designed using Primer3 Input (version 0.4.0) (http://bioinfo.ut.ee/primer3-0.4.0/primer3) and synthesized by Integrated DNA Technologies. Below table showing the list of Oligonucleotide Primers used in the study.

SYBR Green qPCR	**Sequence**
mouse GAPDH FWD	CGACTTCAACAGCAACTCCCACTCTTCC
mouse GAPDH REV	TGGGTGGTCCAGGGTTTCTTACTCCTT
mouse AR FWD	GATGGTATTTGCCATGGGTTG
mouse AR REV	GGCTGTACATCCGAGACTTGTG
mouse TMPRSS2 FWD	GGCCGCTGGTTACTTTGAAG
mouse TMPRSS2 REV	TCGTGTCCCCAATCAGCC
mouse ACEII FWD	GGATACCTACCCTTCCTACATCAGC
mouse ACEII REV	CTACCCCACATATCACCAAGCA
human GAPDH FWD	TGCACCACCAACTGCTTAGC
human GAPDH REV	GGCATGGACTGTGGTCATGAG
human AR FWD	CAGTGGATGGGCTGAAAAAT
human AR REV	GGAGCTTGGTGAGCTGGTAG
human TMPRSS2 FWD	CAGGAGTGTACGGGAATGTGATGGT
human TMPRSS2 REV	GATTAGCCGTCTGCCCTCATTTGT
human ACEII FWD	CATTGGAGCAAGTGTTGGATCTT
human ACEII REV	GAGCTAATGCATGCCATTCTCA

Cell culture

Prostate cancer cell line LNCaP (obtained from ATCC) and lung cancer cell lines H838 and H460 (obtained from ATCC) were maintained in RPMI-1640 media (Gibco, 11875093). Lung cancer

cell line Calu-3 (obtained from ATCC) was maintained in DMEM/F-12 (Gibco, 11320033). HEK-293T cells (obtained from ATCC) and HEK-293T-ACE2cl.22 (Gift from Paul D. Bieniasz, Rockefeller University) were maintained in DMEM media (Gibco, 21013024). The medium was supplemented with 10% of Fetal Bovine Serum (FBS) (HYC, SH30910.03) and 1% of Penicillin Streptomycin Solution (Invitrogen, 15140122), hereto referred to as "complete media". All cell lines were tested negative for mycoplasma contamination, and were maintained in a humidified incubator at 37°C and 5% CO_2.

Drugs/Chemicals

The enzalutamide (Selleckchem, S1250), Camostat Mesylate (Selleck Chemicals, 59721-29-8) and PROTAC-ARD-69 (gift from Dr. Shaomeng Wang, University of Michigan, Ann Arbor, MI, Ref: http://dx.doi.org/10.1021/acs.jmedchem.8b01631) were dissolved and aliquoted in DMSO (Sigma-Aldrich, D2650). 5α-Dihydrotestosterone (Cerilliant, D073) was dissolved and aliquoted in methanol.

Androgen deprivation and Drug treatments

For starvation or DHT stimulation for AR signaling, LNCaP, and H460 cells were plated in complete media at required confluency. After 24h cells were washed with DPBS and cultured in RPMI 1640 without Phenol Red (Invitrogen-11835030) with 10% charcoal-dextran stripped FBS (Gemini Bio-Products- 100119) for 2, 4 and 6 days. Regular RPMI 1640 medium with 10% FBS was included as a control. For drug treatments, the cells after 24h of seeding in complete media were exposed to either 25 μM Enzalutamide or 250 nM PROTAC ARD-69 for 3 and 6 days. Cells treated with DMSO were used as a control. After the treatment time points, the total RNA and protein lysates were prepared for qRT-PCR and immunoblotting, respectively.

Immunoblotting and Co-immunoprecipitation

Cell lysates were prepared with RIPA buffer (Boston Bioproducts, BP-115DG)-10 mM Tris-HCl pH 7.5, 1 mM EDTA, 400 mM NaCl, 0.5% NP-40, and 1 mM DTT, supplemented with protease inhibitor cocktail (Pierce, A32965) and phosphatase inhibitor (Thermo, 1861280). For immunoblotting, the total protein lysates were boiled at 100°C in Laemmli Sample Buffer (Bio-rad, 1610737) and then separated by SDS-PAGE and transferred onto Polyvinylidene Difluoride

membrane (GE Healthcare, IPVH00010). The membrane was incubated for one hour in blocking buffer [Tris-buffered saline, 0.1% Tween (TBS-T), 5% nonfat dry milk] followed by overnight incubation on a rocker at 4°C with the primary antibody. Following a wash with TBS-T, the membrane was incubated with horseradish peroxidase-conjugated secondary antibody for 2h on a rocker at room temperature. The membrane was washed again, and signals were visualized using enhanced chemiluminescence system as per manufacturer's protocol (GE Healthcare) or Kwik Quant Imager (Kindle Biosciences). All antibodies were employed at the dilutions suggested by the manufacturers.

For immunoprecipitation experiments, protein extracts were obtained from cells using IP buffer (20 mM Tris pH7.5, 150 mM NaCl, 1% Triton-X 100, 5mM EDTA, Protease/Phosphatase Inhibitor) by sonication. The lysates (0.35-1.0 mg) were pre-cleaned by incubation with protein G Dyna beads (Thermo Fisher Scientific, 10004D) for 1h on a rotator at 4°C. 2-5 µg antibody per milligrams of protein was added to the pre-cleared lysates and incubated on a rotator at 4°C overnight. Following over-night incubation Protein G Dyna beads were then added for 1h. Beads were washed four times in IP buffer, containing 300 mM NaCl and then resuspended in 40 µL of 2x Laemmli Sample Buffer and then boiled for 10min. Samples were then analyzed by SDS-PAGE and immunoblotting as described above. Antibodies used in the study is provided in the table below.

Antibody	**Application**	**Source**	**Cat. #**
Mouse ACE2	IHC/IB	R&D System	AF3437
Human ACE2	IB	R&D System	AF933
TMPRSS2	IB	Abcam	ab92323
TMPRSS2	IHC/IB	Abcam	ab109131
AR	IHC/IB	Abcam	ab74272
pS81-AR	IB	Millipore	07-1375-EMD
HIV-1 core antigen-RD1, KC57 (p24)	IB	Beckman Coulter Life Sciences	6604667
Streptavidin-tag II	IB	Abcam	ab76950
GAPDH	IB	Cell Signaling Technology	3683S
β-Actin (D6A8)	IB	Cell Signaling Technology	8457S

Gene overexpression studies

Plasmids expressing TMPRSS2 (pCSDest-hTMPRSS2, 53887) and SARS-CoV-2 spike protein (pLVX-EF1alpha-nCoV2019-S-2xStrep-IRES-Puro) were transfected alone or co-transfected into HEK-293T cells using Lipofectamine 2000 (Invitrogen Life Technologies, 12566014) as per manufacturer's protocol. 48-72h post-transfection the cells were harvested and subjected to immunoblotting. See below table for the information on plasmid constructs used in the study.

Plasmid	**Source**	**Cat. #**
pCSDest-hTMPRSS2	Addgene	53887
pLVX-EF1alpha-nCoV2019-S-2xStrep-IRES-Puro	Gordon DE et al. Nature 2020	-
pHIV-1(NL4.3) Env-NanoLuc	Gift from Paul D. Bieniasz, Rockefeller University	-
pSARS-CoV-2-S(D19)	Gift from Paul D. Bieniasz, Rockefeller University	-
VSV-G	Addgene	-

Spinoculation

To evaluate the activity of TMPRSS2 on cell surface-bound SARS-CoV-2 Spike priming, the HIV/NanoLuc SARS-CoV-2 pseudo viral particles were spinoculated to HEK -293T-ACE2cl.22 cells. Prior to this, the cells were seeded in 6 well plates at a 70% confluency and transfected with pCSDest-hTMPRSS2 plasmid for 48h followed by 5h treatment with dmso or Camostat. For spinoculation, the cells were centrifuged in Sorvall Legend XTR Centrifuge (Thermo Scientific) for 1h at 800 x g, 37°C. Next, the cells were washed 2-3 times with the desired medium to remove the residual viral particles and incubated at 37°C and 5% Co2 for 4 more hours. Similarly, to check the effect of the endogenous TMPRSS2 on SARS-CoV-2 spike protein in LNCaP and Calu-3 cell lines, the same protocol was followed except the pCSDest-hTMPRSS2 transfection. After 4h incubation, the protein lysates were prepared, and the cleavage of SARS-CoV-2 Spike protein was analyzed through immunoblotting.

Pseudo virus packaging

To generate HIV/NanoLuc SARS-CoV-2 pseudo viral particles, HEK-293T cells were plated in 10 cm dish in 10ml DMEM + 10% FBS on day 0. Sixteen hours later, cells were starved with 4 ml of serum-free Opti-MEM (Thermo Fisher, 11058021) for 1 h. 6 µg of pHIV-1NL4-3 ΔEnv-NanoLuc reporter virus plasmid and 3 µg of SARS-CoV-2 spike protein plasmid (pSARS-CoV-2-SΔ19 or pLVX-EF1alpha-nCoV2019-S-2x Strep-IRES-Puro) were mixed thoroughly with 500 µl Opti-MEM. 9 µL of Lipofectamine 2000 (Thermo Fisher, 11668019) was diluted in 500 µl Opti-MEM and mixed thoroughly. The plasmid and lipofectamine mixture were incubated together at room temperature for 15min before adding to the cells dropwise. After 8h of incubation, the media was replaced with 10ml of DMEM + 10% of FBS. After 48h and 60h post-transfection, the supernatant was harvested and clarified by centrifugation at 500 x g for 10min and filtered through a 0.45 µm syringe filter (VWR, 28145-481). To concentrate the virus, 1 volume of Lenti-X Concentrator (Takara, 631232) was mixed with 3 volumes of clarified supernatant and incubated at 4°C for 5 h, followed by centrifugation at 1,500 x g for 45min at 4°C. The viral pellet was resuspended in 1/5 of its original volume and stored at –80°C in single-use aliquots. HIV/NanoLuc VSV-G control viral particles were generated by merely replacing Spike S plasmid with VSV-G.

Transduction and Nano-Luciferase Reporter Assay

For SARS-CoV-2 Spike pseudovirus cell entry, 20,000 cells were seeded in 96-well plates on day 0 to achieve 50%-60% of confluency. On day 1, cells were treated with ARD-69 (500 nM), Enzalutamide (10 µM) or camostat mesylate (300 µM), respectively or camostat mesylate in combinations of ARD-69 or Enzalutamide in 50 µL of full media for one hour before transduction. To test effect the of androgen deprivation on transduction efficiency, 20,000 cells were seeded in 96-well plates on day 0 to achieve 50%-60% of confluency. On day 1, we genteelly washed the cells with PBS and changed the media to RPMI + 10% CSS. On day 3, we pretreated the cells with DHT (10 nM) and/or camostat mesylate (300 µM) for one hour before transduction.

For transduction, 50 µL of HIV/NanoLuc VSVG or HIV/NanoLuc SARS-CoV-2 pseudo viral particles were added to each well of the cells. The transduction efficiency (pseudovirus entry) was quantified 24 h post-transduction using Nano-Glo Luciferase Assay System (Promega, N1110). Cells were lysed in 50 µL of buffer for 5 min at room temperature, and then lysates were transferred to white opaque flat-bottom 96-well plates for luminescence reading on BioTek Synergy HT. Relative luminescence units (RLU) obtained were normalized to the values derived from cells

infected with the SARS-CoV-2 pseudovirus with DMSO or DHT+DMSO treatment to present the relative entry efficiency.

Mass Spectrometry Analysis

Streptavidin IP eluate was resolved with SDS-PAGE and visualized with Coomassie stain. Regions corresponding to two prominent bands were excised from the gel and cut into 1 mm^3 cubes. They were destained with 50% Methanol/1.25% Acetic Acid, reduced with 5 mM DTT (Dithiothreitol) (Thermo), and alkylated with 40 mM iodoacetamide (Sigma). Gel pieces were then washed with 20 mM ammonium bicarbonate (Sigma) and dehydrated with acetonitrile (Fisher). Trypsin (Promega) (5 ng/mL in 20 mM ammonium bicarbonate) was added to the gel pieces and proteolysis was allowed to proceed overnight at 37ºC. Peptides were extracted with 0.3% triflouroacetic acid (J.T.Baker), followed by 50% acetonitrile. Extracts were combined and the volume was reduced by vacuum centrifugation.

Samples were analyzed on a QExactive HF mass spectrometer (Thermofisher Scientific San Jose, CA) coupled with an Ultimate 3000 nano UPLC system and EasySpray source. Peptides were separated by reverse phase (RP)-HPLC on Easy-Spray RSLC C18 2 um 75 μm id × 50cm column at 50ºC. Mobile phase A consisted of 0.1% formic acid and mobile phase B of 0.1% formic acid/acetonitrile. Peptides were eluted into the mass spectrometer at 300 nL/min with each RP-LC run comprising a 95-minute gradient from 1 to 3% B in 5 min, 3-45%B in 90 min. The mass spectrometer was set to repetitively scan m/z from 300 to 1800 (R = 120,000) followed by data-dependent MS/MS scans on the twenty most abundant ions, minimum AGC 1e4, dynamic exclusion with a repeat count of 1, repeat duration of 15s, (R=45000) and a NCE of 27. FTMS full scan AGC target value was 5e5, while MSn AGC was 1e5, respectively. MSn injection time was 120 ms; microscans were set at one. Rejection of unassigned, 1, 6-8 and >8 charge states was set.

QA/QC and system suitability

For online monitoring of the QExactive HF instrument, parallel reaction monitoring (PRM) analysis for the spiked-in iRT peptides was performed though Skyline AutoQC, and the data were uploaded and accessed in Skyline Panorama (Bereman et al., 2016). Meanwhile, as a measure for QC/QA, we injected standard E. coli protein digest in between samples (one injection after every

four injections). The collected DDA data were analyzed in MaxQuant. The MaxQuant output was subsequently visualized using the PTXQC package to track the quality of the instrumentation(Bielow et al., 2016).

Search MS raw files

Protein and peptide identification/quantification was performed with MaxQuant (1.6.14.0) using a SARS COVID19 reference database from Uniprot (reviewed canonical and isoforms; downloaded on 20200904). Carbamidomethyl of Cys was defined as a fixed modification. Oxidation of Met and Acetylation of protein N-terminal were set as variable modifications. Trypsin/P was selected as the digestion enzyme, and a maximum of 3 labeled amino acids and 2 missed cleavages per peptide were allowed. Fragment ion tolerance was set to 0.5 Da. The MS/MS tolerance was set at 20 ppm. The minimum peptide length was set at 7 amino acids. The rest of the parameters were kept as default. The MaxQuant results were imported into Scaffold (Proteome Software) for data visualization.

Reference

Bereman, M.S., Beri, J., Sharma, V., Nathe, C., Eckels, J., MacLean, B., and MacCoss, M.J. (2016). An Automated Pipeline to Monitor System Performance in Liquid Chromatography-Tandem Mass Spectrometry Proteomic Experiments. J Proteome Res *15*, 4763-4769.

Bielow, C., Mastrobuoni, G., and Kempa, S. (2016). Proteomics Quality Control: Quality Control Software for MaxQuant Results. J Proteome Res *15*, 777-787.

Consortium, G.T., Laboratory, D.A., Coordinating Center -Analysis Working, G., Statistical Methods groups-Analysis Working, G., Enhancing, G.g., Fund, N.I.H.C., Nih/Nci, Nih/Nhgri, Nih/Nimh, Nih/Nida*, et al.* (2017). Genetic effects on gene expression across human tissues. Nature *550*, 204-213.

Heinz, S., Benner, C., Spann, N., Bertolino, E., Lin, Y.C., Laslo, P., Cheng, J.X., Murre, C., Singh, H., and Glass, C.K. (2010). Simple combinations of lineage-determining transcription factors

prime cis-regulatory elements required for macrophage and B cell identities. Mol Cell *38*, 576-589.

Zhang, Y., Liu, T., Meyer, C.A., Eeckhoute, J., Johnson, D.S., Bernstein, B.E., Nusbaum, C., Myers, R.M., Brown, M., Li, W.*, et al.* (2008). Model-based analysis of ChIP-Seq (MACS). Genome Biol *9*, R137.